

Photodissociation of carbon dioxide in singlet valence electronic states. II. Five state absorption spectrum and vibronic assignment

Sergy Yu. Grebenshchikov*

*Department of Chemistry, Technical University of Munich,
Lichtenbergstr. 4, 85747 Garching, Germany*

The absorption spectrum of CO₂ in the wavelength range 120 nm — 160 nm is analyzed by means of quantum mechanical calculations performed using vibronically coupled PESs of five singlet valence electronic states and the coordinate dependent transition dipole moment vectors. The thermally averaged spectrum, calculated for $T = 190$ K via Boltzmann averaging of optical transitions from many initial rotational states, accurately reproduces the experimental spectral envelope, consisting of a low and a high energy band, the positions of the absorption maxima, their FWHMs, peak intensities, and frequencies of diffuse structures in each band. Contributions of the vibronic interactions due to Renner-Teller coupling, conical intersections, and the Herzberg-Teller effect are isolated and the calculated bands are assigned in terms of adiabatic electronic states. Finally, diffuse structures in the calculated bands are vibronically assigned using wave functions of the underlying resonance states. It is demonstrated that the main progressions in the high energy band correspond to consecutive excitations of the pseudorotational motion along the closed loop of the CI seam, and progressions differ in the number of nodes along the radial mode perpendicular to the closed seam. Irregularity of the diffuse peaks in the low energy band is interpreted as a manifestation of the carbene-type ‘cyclic’ OCO minimum.

I. INTRODUCTION

This paper describes the results of an ab initio quantum mechanical study of the absorption spectrum of carbon dioxide photoexcited with the ultraviolet (UV) light between

* Sergy.Grebenshchikov@ch.tum.de

120 nm and 160 nm and offers vibronic assignments of the diffuse absorption bands. A brief account of this work has already been published.¹ The potential energy surfaces (PESs) used in these calculations are described in the preceding paper (termed ‘paper I’).²

Photodissociation of carbon dioxide is of considerable importance for atmospheric and planetary chemistry. CO₂ is the second common trace gas in the Earth atmosphere and one of the main products of the fossil fuel burning. Its emissions continue to grow³ despite considerable effort to mitigate climate change.^{4,5} UV photodissociation destroys CO₂ with a unit quantum yield, and in the upper atmosphere, this destruction channel is dominant. Photolysis, shifted into the UV/visible range via preheating of CO₂, has been used in solar based schemes of conversion of atmospheric CO₂ into fuel.^{6,7} UV photochemistry of carbon dioxide controls chemical processes in the upper layers of the CO₂ based atmospheres of Mars and Venus.⁸ Accurate predictions of the low temperature UV absorption cross sections are required to improve the existing photochemical models of their atmospheres, and are also relevant for the models of the atmosphere of Titan,⁹ which contains CO₂ as a minor constituent. Finally, photodissociation shares its activated complex — the highly electronically and vibrationally excited CO₂ — with another reaction, in which C + O₂ collisions produce carbon monoxide, the second most abundant molecule in interstellar clouds.¹⁰

Absorption spectrum of CO₂ in the UV range is studied experimentally since the beginning of the 20th century.^{11–18} Figure 1(a) gives an overview between 220 nm and 105 nm. Carbon dioxide is transparent down to about 220 nm (6.20 eV). Below 220 nm, the absorption starts with a very weak progression of narrow lines.^{14,19,20} At 112.1 nm (11.08 eV), a strong absorption band is observed, which is assigned^{15,21} to the optically allowed transition to the Rydberg state $^1\Sigma_u^+$; this band is the first in a series of Rydberg transitions at shorter wavelengths [not shown in Fig. 1(a)]. Between 160 nm and 120 nm (7.75 eV — 10.33 eV), two relatively weak absorption bands are located, with the stronger one centered at 133 nm (9.30 eV) and the weaker one at 148 nm (8.40 eV). Magnified view of this spectral interval is given in Fig. 1(b). Each band exhibits irregular diffuse structures superimposed on broad structureless background. The vibronic origin of the diffuse structures and the dissociation mechanisms in these two bands are subjects of this paper.

Previous analysis established key electronic states in the observed spectrum.^{13,15,22–26} These are the singlet valence states $2, 3^1A'$ and $1, 2, 3^1A''$, properties and topographies of the global PESs of which are discussed in paper I. It is customary to give electronic assignment

using the $D_{\infty h}$ labels, appropriate for linear CO₂, namely $1^1\Sigma_u^-$, $1^1\Pi_g$, and $1^1\Delta_u$, with the low energy band at 148 nm assigned to the $1^1\Delta_u$ state, and the high energy 133 nm band to the $1^1\Pi_g$ state.^{13,15,22} However, the interstate vibronic couplings calculated in paper I are strong rendering such ‘zeroth order’ diabatic labels somewhat problematic. Vibrational progressions are isolated using solely line spacings. For the stronger lines near 133 nm, one bending or two stretching progressions are offered as alternative tentative assignments.^{15,27} The weaker band near 148 nm is presumed to involve strong bending excitations. This assignment is based on the analysis of Dixon²² who characterized the upper state in the 148 nm transition as bent (two-dimensional contour maps of the lowest two bent excited states $2^1A'$ and $1^1A''$ are shown in Figs. 9 and 13 of paper I). However, the intervals between diffuse peaks are strongly perturbed and rather irregular in both absorption bands: A unequivocal assignment is difficult without a convincing spectroscopic model or accurate dynamics calculations.

Irregularities in the peak spacings and intensity distributions are due to strong vibronic interactions, rooted in the symmetry properties of the excited valence states. In the near linear Franck-Condon (FC) region, vibronic effects can be grouped into three classes:

(1) The rotoelectronic Renner-Teller (RT) effect involves A' and A'' components of the orbitally degenerate $1^1\Pi_g$ or $1^1\Delta_u$ state. Figure 2(a) illustrates how the degeneracy is lifted as CO₂ bends. In the shown cut, the upper two states stem from $1^1\Pi_g$, the lower two stem from $1^1\Delta_u$, and the transitions $1^1\Pi_g \leftarrow \tilde{X}^1\Sigma_g^+$ and $1^1\Delta_u \leftarrow \tilde{X}^1\Sigma_g^+$ can be nominally classified as linear-linear and linear-bent, respectively. In either case, the A'/A'' interaction $\sim \Lambda\Omega/\sin^2\alpha_{\text{OCO}}$ is proportional to the projections Λ and Ω of the electronic (\hat{L}) and the total angular momentum ($\hat{J} = \hat{N}_{\text{CO}_2} + \hat{L}$) on the molecular axis and, for $\Omega \neq 0$, diverges as $\alpha_{\text{OCO}} \rightarrow 180^\circ$.^{13,28–30} If \hat{J} is normal to the CO₂ axis and $\Omega = 0$, the RT coupling is quenched. Interaction between A' and A'' states in this case is mediated only by the Coriolis coupling which allows transitions from $\Omega = 0$ to $\Omega = 1$ block in which RT coupling is operative.

(2) The symmetry allowed conical intersections (CIs) occur between states $1^1\Delta_u$ and $1^1\Pi_g$; two avoided crossings in Fig. 2(b) near $2.2a_0$ and $2.9a_0$ illustrate positions of the CIs. Calculations detect CIs for two A' states, $2^1A'$ and $3^1A'$, and two A'' states, $1, 2^1A''$ or $2, 3^1A''$. In both symmetry blocks, the degeneracies are lifted linearly as the molecule bends or as one CO bond is extended. The two intersections, implied in Fig. 2(b), are not independent: They belong to a single ‘CI seam’ in the (R_1, R_2) plane of the CO bond distances in linear OCO. The CI seam forms a closed loop as discussed in Sect. III C of paper I and in Ref.

31. In fact, the closed CI seam is a line of fivefold degeneracy which passes through the FC region. Calculations discussed below demonstrate that the closed seam substantially affects vibronic eigenstates located above the CIs in the strong absorption band at 133 nm.

(3) The Herzberg-Teller (HT) effect¹³ is seen as a strong coordinate dependence of the transition dipole moments (TDMs) with \tilde{X} . The TDM vectors in the principal axes system are shown in Fig. 3 as functions the CO bond length and the OCO angle.³² Although the HT interaction neither requires nor involves a direct state intersection, its effect upon the intensity distribution in the spectrum is virtually indistinguishable from that of a CI in the FC region. Optical transitions from $\tilde{X}^1\Sigma_g^+$ to the states $1^1\Sigma_u^-$, $1^1\Pi_g$, and $1^1\Delta_u$ are forbidden in the $D_{\infty h}$ symmetry group. The TDM along the molecular axis, μ_y , transforms according to the irrep $\Gamma^{\mu_y} = \sigma_u^+$, while the components μ_x and μ_z are of $\Gamma^{\mu_x} = \Gamma^{\mu_z} = \pi_u$ symmetry. Direct products^{33,34} $\Gamma_i^{\text{el}} \times \Gamma^\mu \times \Gamma_f^{\text{el}}$ of these irreps with the electronic symmetries $\Gamma_i^{\text{el}} = \Sigma_g^+$ and $\Gamma_f^{\text{el}} = \Sigma_u^-, \Pi_g$, or Δ_u are never totally symmetric and all TDMs at the FC point vanish. Transitions become vibronically allowed in distorted molecule, and the TDMs directly depend on displacements in non-totally symmetric coordinates. The observed absorption between 120 nm and 160 nm is entirely due to this coordinate dependence. For linear deviations from $D_{\infty h}$, active in the transitions are the antisymmetric stretch $R_- = (R_1 - R_2)/\sqrt{2}$ (irrep σ_u^+) and the bend α_{OCO} (irrep π_u). In linear CO_2 , the components $\mu_{x,z}$ are antisymmetric with respect to R_- as illustrated in Fig. 3(a,c). The component μ_y grows linearly with α_{OCO} , while $\mu_{x,z}$ are almost independent of the OCO angle [Fig. 3(d,e,f)]. The TDM components corresponding to states $1^1\Sigma_u^-$ and $1^1\Delta_u$ are easily identified at linearity [Fig. 3(a,c)] by their small absolute values; the transition to $1^1\Pi_g$ dominates in $C_{\infty v}$. The coordinate dependence of the TDMs, violating both the Born-Oppenheimer and the FC approximations,^{13,35} is commonly ascribed to the ‘intensity borrowing’ from an adjacent bright lender state. The nearest bright state which might contribute to the vibronically induced TDMs in Fig. 3 is the Rydberg state $1^1\Sigma_u^+$ lying almost 2 eV above $1^1\Pi_g$. As deviations from $D_{\infty h}$ grow, higher than linear expansion terms contribute, all TDM components become nonzero, and all states can be excited in the bent molecule [Fig. 3(d,e,f)]. The A' states are excited via the in-plane components $\mu_{y,z}$. The out-of-plane component μ_x mediates excitation of the A'' states. The symmetry of $\mu_{x,y,z}$ in Fig. 3 implies that parallel (perpendicular) transitions excite vibrational states which are symmetric (antisymmetric) with respect to interchange, $R_1 \leftrightarrow R_2$, of the two CO bonds.

In this paper, the absorption spectrum of CO₂ is calculated using ab initio PESs of the first five excited electronic states, vibronic interstate couplings, and multistate quantum dynamics for the nuclei. The study was designed with three goals in mind: To reproduce the experimental spectrum, to assign the calculated absorption bands, and to examine the relative contributions of the above non-adiabatic interactions. These tasks are connected, because photoexcitation brings CO₂ into the region of multiple degeneracies (Fig. 2), and all low lying states, populated via the HT effect, might be interlinked through an intricate network of couplings created at the RT intersections and the CIs. A realistic assignment should reflect the extent of this mixing. The outline of the paper is as follows: The multistate quantum mechanical calculations of the absorption spectrum and resonances in dissociation continua of the five excited electronic states are summarized in Sect. II. The calculated spectrum is compared with experiment and assigned in Sect. III. Individual rotoelectronic transitions are isolated in Sect. III A allowing ‘coarse grained’ electronic assignment of the two calculated bands and a qualitative assessment of the role of RT coupling. Section III B assigns vibronic progressions in the stronger high energy band and shows that nodal lines of resonance wave functions follow the topography of the upper adiabatic PESs near the closed CI seam. Vibronic assignments of the low energy band, much less definitive because of strong anharmonic and vibronic couplings, are discussed in Sect. III C. Weak absorption of the state $1^1\Sigma_u^-$ is the subject of Sect. III D. Summary is given in Sect. IV.

II. QUANTUM MECHANICAL CALCULATIONS

A. Molecular Hamiltonian

The starting point for the calculations is the 5×5 molecular Hamiltonian written in the basis of the electronic states $|\Delta'\rangle$, $|\Pi'\rangle$, $|\Sigma''\rangle$, $|\Pi''\rangle$, and $|\Delta''\rangle$, diabaticized with respect to CIs at bent geometries and in the FC region as described in Sect. IV B of paper I:

$$\mathbf{H}_0 = \mathbf{T} + \mathbf{S}^T \mathbf{V}^a \mathbf{S} = \mathbf{T} + \mathbf{V}^d, \quad (1)$$

with the nuclear kinetic energy matrix \mathbf{T} and the potential matrix \mathbf{V}^d , related to the diagonal matrix of ab initio energies \mathbf{V}^a via orthogonal adiabatic-to-diabatic (ADT) transformation \mathbf{S}

and consisting of a 2×2 block of A' and a 3×3 block of A'' states:

$$\mathbf{V}^d = \left(\begin{array}{cc|ccc} V_{\Delta'} & V_{\Pi'\Delta'} & & & & \\ V_{\Pi'\Delta'} & V_{\Pi'} & & & & \\ \hline & & V_{\Sigma''} & V_{\Sigma''\Pi''} & V_{\Sigma''\Delta''} & \\ & & V_{\Sigma''\Pi''} & V_{\Pi''} & V_{\Pi''\Delta''} & \\ & & V_{\Sigma''\Delta''} & V_{\Pi''\Delta''} & V_{\Delta''} & \end{array} \right). \quad (2)$$

All matrix elements are smooth functions of molecular coordinates; couplings of the accidentally degenerate states $|\Sigma''\rangle$ and $|\Delta''\rangle$ to $|\Pi''\rangle$ are set equal, and the RT-like Σ''/Δ'' interaction is neglected. This representation will hereafter be referred to as CI-diabatic; by construction, the projection of \hat{L} on the molecular figure axis, \hat{L}_z^2 , in the CI-diabatic basis has a definite value of $\Lambda = 0, 1$, or 4 . The kinetic energy operator \hat{T} is specified in the body fixed (BF) frame in Jacobi coordinates (R, r, γ) in the form, originally suggested by Petrongolo²⁹ and modified for numerical implementations by Goldfield et al.³⁰

$$\begin{aligned} \hat{T} = & \left[\hat{T}_R + \hat{T}_r + (B_R + B_r) \left(\hat{T}_\gamma + \frac{\hat{j}_z^2 + \hat{L}_z^2}{\sin^2 \gamma} \right) + B_R \left(\hat{J}^2 - 2\hat{J}_z^2 - \hat{L}_z^2 \right) \right] \\ & - \left[2(B_R + B_r) \frac{\hat{J}_z \hat{L}_z}{\sin^2 \gamma} - 2B_R \hat{J}_z \hat{L}_z \right] + \left[B_R \hat{J}_+ \hat{j}_- + B_R \hat{J}_- \hat{j}_+ \right]. \end{aligned} \quad (3)$$

Jacobi coordinates in this expression comprise the distance R between one oxygen atom and the center of mass of CO, the CO distance r , and the angle γ between the vectors \mathbf{R} and \mathbf{r} . Operators \hat{T}_R , \hat{T}_r , and \hat{T}_γ are the standard³⁶ kinetic energies for these coordinates; the rotational constants $B_R = (2\mu_R R^2)^{-1}$ and $B_r = (2\mu_r r^2)^{-1}$ depend on the corresponding reduced masses $\mu_{R,r}$. \hat{J} denotes the total angular momentum, $\hat{J} = \hat{N}_{\text{CO}_2} + \hat{L}$ (\hat{N}_{CO_2} is the angular momentum of nuclei). \hat{J}_z and \hat{J}_\pm denote the BF z projection and the ladder operators of \hat{J} , respectively. The BF z axis is assumed to run parallel to \mathbf{R} ('R-embedding', Ref. 37); finally, $\hat{j}_\pm = (\hat{J}_z - \hat{L}_z) \cot \gamma \mp \partial/\partial\gamma$. In the basis of CI-diabatic states, the first bracket in Eq. (3) applies to the vibronic dynamics in either A' or A'' symmetry block; the second bracket is the RT interaction between A' and A'' states sharing the same Λ^2 ; the third bracket is the Coriolis interaction which includes both intra-symmetry (through e.g. $\hat{J}_+ \hat{J}_z$ terms) and inter-symmetry (through e.g. $-\hat{J}_+ \hat{L}_z$ terms) couplings.

Divergence at $\gamma \rightarrow 0, \pi$ of the kinematic RT coupling matrix elements for states with $\Lambda^2 \neq 0$ is removed by switching from the definite symmetry states $|\Lambda'\rangle$ and $|\Lambda''\rangle$ to the

RT-diabatic eigenstates $|\Lambda^\pm\rangle$ of the \hat{L}_z operator at linearity,³⁰

$$|\Lambda^\pm\rangle = \frac{1}{\sqrt{2}} (|\Lambda'\rangle \pm i|\Lambda''\rangle); \quad (4)$$

Applied to Eq. (2), this transformation gives a full CI/RT-diabatic representation, with all kinematic couplings replaced with potential matrix elements. The matrix \mathbf{V}^d loses its block diagonal form and comprises three groups of elements: (1) Diagonal CI/RT-diabatic ‘potentials’ $\frac{1}{2}(V_{\Lambda'} + V_{\Lambda''})$, (2) off-diagonal vibronic couplings due to CIs involving states with $\Lambda_1 \neq \Lambda_2$, $\frac{1}{2}(V_{\Lambda'_1\Lambda'_2} + V_{\Lambda''_1\Lambda''_2})$, and (3) off-diagonal rotovibronic couplings $\frac{1}{2}(V_{\Lambda'} - V_{\Lambda''})$ due to RT effect. The state $|\Sigma''\rangle$, vibronic couplings for which are set equal to those of $|\Delta''\rangle$ and the RT effect is absent, becomes decoupled from other states in this approximation.

The rotoelectronic basis in which the molecular Hamiltonian is set consists of direct products $\{|\Theta_{M\Omega}^J\rangle|\Lambda^\pm\rangle\}$ of the electronic CI/RT-diabatic functions and the rotational basis functions $|\Theta_{M\Omega}^J\rangle$ expressed via Wigner D matrices; M denotes the space-fixed and Ω the body-fixed projection of J . In the actual implementation, this basis is further transformed by taking parity adapted linear combinations^{30,36} of basis functions with $\pm|l| = \pm(\Omega + \Lambda)$ or $\pm|l| = \pm(\Omega - \Lambda)$. Further, the Jacobi angle is discretized and the angular differential operators are set in the Gauss-associated Legendre discrete variable representation (DVR). Finite basis representation is kept only in the quantum numbers Ω and Λ .

B. The initial state and the absorption spectrum

CO₂ in the rotational state (J_i, Ω_i) in $\tilde{X}^1\Sigma_g^+$ is described by the wave function

$$\Psi_X(\mathbf{q}|J_i, \Omega_i) = \psi_0^{J_i, \Omega_i}(\mathbf{q})|\Theta_{M\Omega_i}^{J_i}\rangle. \quad (5)$$

Here $\psi_0^{J_i, \Omega_i}(\mathbf{q})$ is a given vibrational state and \mathbf{q} denotes three internal (e.g. Jacobi) coordinates. Since \tilde{X} is a Σ state, the initial total angular momentum J_i coincides with the nuclear angular momentum N_{CO_2} . Centrifugal sudden (CS) Coriolis-free approximation is used in Eq. (5) treating CO₂ as a symmetric top with conserved helicity Ω_i . Only excitations from the vibrational ground state are considered, which for linear CO₂ implies $\Omega_i = 0$, too.

The state of CO₂ immediately after photoexcitation is first set in the CI-diabatic representation. TDMS with \tilde{X} are obtained from ab initio TDMS using the ADT matrix \mathbf{S} :

$$\boldsymbol{\mu}^d = (\boldsymbol{\mu}_{\Delta'}^d, \boldsymbol{\mu}_{\Pi'}^d, \boldsymbol{\mu}_{\Sigma''}^d, \boldsymbol{\mu}_{\Pi''}^d, \boldsymbol{\mu}_{\Delta''}^d)^T = \mathbf{S}^T \boldsymbol{\mu}^a = \mathbf{S}^T (\boldsymbol{\mu}_{2A'}^a, \boldsymbol{\mu}_{3A'}^a, \boldsymbol{\mu}_{1A''}^a, \boldsymbol{\mu}_{2A''}^a, \boldsymbol{\mu}_{3A''}^a)^T, \quad (6)$$

The resulting TDM ‘vector’ has five electronic components, each featuring up to two non-vanishing spatial projections in the principal axes frame. Possible rotational transitions in the optical excitation are $J_i \rightarrow J_f = J_i, J_i \pm 1$ and $\Omega_i = 0 \rightarrow \Omega_f = 0, 1$ (parallel case) or $\Omega_i = 0 \rightarrow \Omega_f = 1$ (perpendicular case). Parallel and perpendicular transitions are calculated separately. The electronic component of the initial excitation in the CI-diabatic state Λ with the angular momentum J_f and the BF projection Ω_f reads as

$$\Phi(\mathbf{q}|J_f, \Omega_f)_\Lambda = \langle 1\delta, J_i 0 | J_f \Omega_f \rangle (\mu_\Lambda^d)_\delta \psi_0^{J_i, 0}(\mathbf{q}) |\Theta_{(m+M)\Omega_f}^{J_f}\rangle, \quad (7)$$

Here $\langle \cdot, \cdot | \cdot \rangle$ is the Clebsh-Gordon coefficient, $\delta \equiv \Omega_f - \Omega_i = 0$ or 1 , and $(\mu_\Lambda)_\delta$ are the spherical projections of the TDM vectors $\boldsymbol{\mu}_\Lambda$: $(\mu)_{\delta=0} = \mu_z$ and $(\mu)_{\delta=\pm 1} = -(\mu_y - i\mu_x)/\sqrt{2}$. This expression is valid for both parallel and perpendicular transitions. The only difference between the two is that the initial state in a parallel transition is real, while in a perpendicular transition it is imaginary. For each type of transition, the total initial wavefunction $\Phi(\mathbf{q}|J_f)$ is a linear combination of all $\Phi(\mathbf{q}|J_f, \Omega_f)_\Lambda$ with the allowed values of Λ and (J_f, Ω_f) .³⁸ Initial state with each J_f is propagated separately. The corresponding cross section, averaged over the initial space fixed projections M , is proportional to the expectation value of the Green’s function of the time-independent Schrödinger equation,³⁹

$$\sigma(E_{\text{ph}}|J_f \leftarrow J_i) = \frac{\pi E_{\text{ph}}}{3c\epsilon_0 \hbar} \langle \Phi(\mathbf{q}|J_f) | \text{Im}G^+(E_{\text{ph}}) | \Phi(\mathbf{q}|J_f) \rangle, \quad (8)$$

where the photon energy E_{ph} is measured from the zero point energy level $E_0(J_i, \Omega_i = 0)$ in \tilde{X} . The total cross section is the sum over all allowed J_f :

$$\sigma(E_{\text{ph}}|J_i) = \overline{\sum_{J_f} \sigma(E_{\text{ph}}|J_f \leftarrow J_i)}. \quad (9)$$

The calculations including all Ω_f blocks for each J_f and thus fully including Coriolis coupling between adjacent helicity blocks were performed for $J_i \leq 2$.

In order to compare the calculation with experiment at $T = 190 \text{ K}$, a thermal absorption spectrum has been constructed by averaging $\sigma(E_{\text{ph}}|J_i)$ over the normalized Boltzmann population $P_{J_i}(T)$ of the initial states J_i ,

$$\sigma(E_{\text{ph}}, T) = \sum_{J_i} P_{J_i}(T) \sigma(E_{\text{ph}}|J_i). \quad (10)$$

Because of large $J_i \leq 45$ involved in these calculations, CS approximation was applied, the Coriolis coupling neglected, and each initial state $\Phi(\mathbf{q}|J_f, \Omega_f)$ processed separately. For $J_i \leq 2$, the spectra obtained with and without CS approximation are in excellent agreement.

In practice, calculations of the absorption spectrum via Eq. (8) are performed in several steps. The CI-diabatic initial state $\Phi(\mathbf{q}|J_f)$ is transformed, first to the CI/RT-diabatic and then to the parity adapted representation. The last transformation is dropped in the CS approximation. Next, the outgoing boundary conditions are approximately imposed in the asymptotic region by augmenting $\hat{\mathbf{H}}_0$ with a complex absorbing potential $-iW$ ($\text{Re } W > 0$):⁴⁰

$$\hat{\mathbf{H}} = \hat{\mathbf{H}}_0 - iW \mathbf{1}. \quad (11)$$

Here $\mathbf{1}$ denotes the 5×5 unit matrix, and one coordinate function W is used in all electronic channels. In the last step, the vector $\text{Im } G^+(E) \Phi(\mathbf{q}|J_f)$ is approximated by the expansion

$$\text{Im } G^+(E) \Phi(\mathbf{q}|J_f) \simeq \sum_{n=0}^{N_{\text{iter}}} [\text{Re } b_n(E)] \Phi_n, \quad (12)$$

in which $b_n(E)$ are the usual energy-dependent coefficients,⁴¹ while the vectors Φ_n are found from a modified Chebyshev recursion relation due to Mandelshtam and Taylor.⁴² Chebyshev autocorrelation coefficients $c_n = \langle \Phi_0 | \Phi_n \rangle$ with the initial state $\Phi_0 \equiv \Phi(\mathbf{q}|J_f)$ are calculated, and the absorption spectrum is reconstructed from $\{c_n\}$ using the Eq. (8). The number of expansion terms, N_{iter} , is one of the convergence parameters of the calculation.

In order to assign diffuse peaks in the spectrum, filter diagonalization^{39,43} has been performed. Eq. (12) is used to generate a set of basis vectors $\{\psi_k\}$,

$$\psi_k = \text{Im } G^+(E_k) \Phi_0, \quad (13)$$

localized around nodes $\{E_k\}$ of an equidistant energy grid covering a given window $[E_{\text{min}}, E_{\text{max}}]$ (500 cm^{-1} wide windows were used in most calculations). The Hamiltonian matrix $\langle \psi_k | H | \psi_{k'} \rangle$ is set in the orthogonalized basis and diagonalized. The resulting complex eigenstates are resonance states of the Hamiltonian (11) with energy E_n and width Γ_n . The eigenfunctions Ψ_n are five component vectors known in any representation used in the calculations. For example, the CI-diabatic eigenstate, $\Psi_n = (\Psi_n^{\Delta'}, \Psi_n^{\Pi'}, \Psi_n^{\Sigma''}, \Psi_n^{\Pi''}, \Psi_n^{\Delta''})^T$, can be rewritten in the CI-adiabatic representation using the ADT matrix via $\mathbf{S}^T \Psi_n$.

C. Numerical details

Quantum mechanical calculations have been performed with several sets of the diabatic PESs constructed using slightly different fitting procedures for ADT parameters as

described in Sect. IVB of paper I. All diabatic sets give indistinguishable absorption spectra. Hamiltonian is set in DVR⁴⁴ with the grid comprising 150 potential-optimized⁴⁵ points in $R \in [1.5, 7.0] a_0$, 100 potential-optimized points in $r \in [1.5, 6.5] a_0$, and $N_\gamma = 100$ Gauss-associated Legendre quadrature points in angle. The grid is contracted by retaining only the points with potential energy below $V_{\text{cut}} = 12.5$ eV above equilibrium in \tilde{X} . $N_{\text{iter}} = 15\,000$ Chebyshev iterations are sufficient to converge the absorption spectrum. The complex absorbing potential $-iW$ is set via a coordinate dependent damping function γ ,⁴² which is zero in the inner parts of the five adiabatic potentials and grows quadratically as a function of CO \cdots O distance in the asymptotic regions. The quadratic polynomial $\gamma(Q)$ ($Q = R$ or r) is described in Refs. 39 and 46. It becomes non-zero $1.1 a_0$ before the grid edge and reaches the strength of 0.15 at the edge.

Temperature dependent absorption cross section is based on spectra calculated for all initial J_i between 0 and 45, the range sufficient for temperatures up to at least $T \sim 250$ K.

Filter diagonalization is performed in several overlapping energy windows covering the photon energy interval from $60\,000 \text{ cm}^{-1}$ to $80\,000 \text{ cm}^{-1}$. Calculated resonances are broad, with the average width of $\bar{\Gamma}_n \geq 50 \text{ cm}^{-1}$, and require 25 000 Chebyshev iterations for convergence. As discussed in Sect. IIIB, the calculated resonances allow a qualitatively accurate reconstruction of the absorption spectrum. All quantum mechanical calculations in this work are performed using the program package ‘PolyWave’.⁴⁷

III. RESULTS

The absorption spectrum, thermally averaged at $T = 200$ K, is compared with the experimental cross section in Fig. 1(b). The calculated spectrum has a characteristic two-band shape, and the band centers at 8.43 eV (147.2 nm) and 9.28 eV (133.6 nm) are accurate within 0.05 eV. The maximum cross sections in the two bands, $5.0 \times 10^{-19} \text{ cm}^2$ and $9.5 \times 10^{-19} \text{ cm}^2$, are about 15% below the experimental values, but the observed 1:2 intensity ratio between the weaker and the stronger band is accurately reproduced. In both spectra, structures in the weaker 148 nm band are substantailly more diffuse and less regular than in the better resolved stronger 133 nm band. Large discrepancies are found in the spectral widths (FWHMs). For the low and the high energy band, FWHMs are 7500 cm^{-1} and 6100 cm^{-1} , i.e. off by 6% and 18% as compared to the respective values of 7000 cm^{-1} and 7400 cm^{-1}

obtained from deconvolution of the experimental spectrum of Ref. 16. The exaggerated gap between the two calculated bands is one of the reasons for this deviation. The gap depth, only weakly dependent on diabaticization details,^{1,2} is sensitive to the TDM derivatives with respect to molecular coordinates at the FC point. In several test calculations, these derivatives — the manifestations of the HT effect — were artificially modified, and the angular derivative $\partial \mu_y / \partial \alpha_{\text{OCO}}$ had the largest impact on the band intensities and the gap size.

The impact of thermal averaging can be assessed by comparing the 200 K spectrum in Fig. 1(b) with the ‘0 K’ spectrum, $\sigma(E_{\text{ph}}|J_i = 0)$, calculated for a single initial rotational state $J_i = 0$ and shown in Fig. 4(a). The differences in positions and maximum intensities are marginal: The 200 K spectrum is red shifted by $\sim 100 \text{ cm}^{-1}$ and its intensity is about 12% higher. Boltzmann averaging primarily affects the extent of spectral fluctuations which in the 200 K spectrum is substantially attenuated. The reason is the inhomogeneous broadening in the spectrum ‘assembled’ from an incoherent average over many spectra for different rotational states J_i . Narrowly spaced and erratically fluctuating lines in the low energy band are more amenable to thermal ‘washing out’ than the well resolved peaks in the high energy band, and the temperature effect is most conspicuous below 9 eV.

A. Electronic assignments

The currently prevailing assignment, attributing the 148 nm band to $1^1\Delta_u$ state and the 133 nm band to $1^1\Pi_g$ state,^{13,15,24} is somewhat ambiguous because these states cross in the FC region. Moreover, this assignment clearly refers to linear geometries because CI-diabatic picture is explicitly selected as a reference. Quantum mechanical approach offers direct means to clarify the electronic origin of each band. For example, the assignments in Ref. 1 were determined using population patterns of the electronic components of resonance wave functions Ψ_n . The results indicate that it is the CI-adiabatic representation which is adequate for the assignment of resonances, implying a strong vibronic coupling scenario:⁴⁸ The $2^1A'$ and $1^1A''$ adiabatic components are strongly populated below the CIs, while the components $3^1A'$ and $3^1A''$ become dominant above the CIs. However, the population analysis works best if the electronic states involved are all bound or all unbound. If, as in the present case, the molecule is excited into the energy range in which the linear states $3^1A'/3^1A''$ are effectively bound, while the bent states $2^1A'/1^1A''$ are dissociative, the results might become

sensitive to the precise definition of the ‘inner region’ used to evaluate electronic populations.

The CI-adiabatic assignments of Ref. 1 can be corroborated using short-time dynamics — a natural approach to establish the electronic labels which refer to the largest energy scale (i.e. the smallest time scale) in the molecule. To this end, two auxiliary diabatic TDM vectors are constructed using the ADT of Eq. (6), one exclusively from the TDMs of the bent adiabatic states $2^1A'/1^1A''$ (termed $\boldsymbol{\mu}_{21}^d$) and the other exclusively from the TDMs of the linear adiabatic states $3^1A'/3^1A''$ (termed $\boldsymbol{\mu}_{33}^d$):

$$\boldsymbol{\mu}_{21}^d = \mathbf{S}^T (\boldsymbol{\mu}_{2A'}^a, 0, \boldsymbol{\mu}_{1A''}^a, 0, 0)^T \quad (14)$$

$$\boldsymbol{\mu}_{33}^d = \mathbf{S}^T (0, \boldsymbol{\mu}_{3A'}^a, 0, 0, \boldsymbol{\mu}_{3A''}^a)^T. \quad (15)$$

For each auxiliary diabatic TDM, the initial excitation, constructed using Eq. (7) for $J_i = 0$, is propagated under the full Hamiltonian for 500 Chebyshev iterations corresponding to a time interval of ~ 0.1 fs. The resulting low resolution spectra are shown in the upper part of Fig. 4(b). They provide a pictorial decomposition of the full spectrum $\sigma(E_{\text{ph}}|J_i = 0)$ into the components due to excitations via $\boldsymbol{\mu}_{21}^d$ and $\boldsymbol{\mu}_{33}^d$. Although not quantitative, the result is clearly consistent with the previous assignment of the 148 nm band to the bent pair $2^1A'/1^1A''$ and the 133 nm band to the linear pair $3^1A'/3^1A''$.

The CI-adiabatic assignment is also motivated by the shape of the initial excitation along the bending angle, sketched in Fig. 2(a) together with the cuts through the calculated PESs. The dashed red line is the ground vibrational state in \tilde{X} . Its maximum is shifted by 4° away from linearity due to the zero-point bending vibration plus the weighting imposed by the volume element. Thus, even before the TDM with the excited states is applied to $\psi_0^{1,0}(\mathbf{q})$, the FC geometry corresponds to $\alpha_{\text{OCO}} = 176^\circ$, and the gap between the adiabatic linear and bent excited states is ~ 0.6 eV. The solid red line in Fig. 2(a) exemplifies the influence of the TDM. Shown is the initial excitation created in the state $3^1A'$ via the TDM μ_y (the initial excitation in $2^1A'$ looks very similar). μ_y strongly depends on angle because of the HT effect, as shown in Fig. 3(e). As a result, the non-vertical transition bends the molecule even stronger, shifting the probability maximum to $\alpha_{\text{OCO}} = 173^\circ$. The linear/bent gap at this angle becomes 0.86 eV and matches the energy separation between the maxima of the two absorption bands (0.85 eV). In fact, the adiabatic gap is a primary control handle of the positions of the band maxima: If the original potentials are modified to reduce the gap size step by step, the bands gradually approach each other and eventually merge.

While vibronic couplings and the HT effect directly shape the UV absorption of CO₂, the role of the rotoelectronic RT coupling is more subtle. The lower part of Fig. 4(b) shows the parallel, σ_{\parallel} , and perpendicular, σ_{\perp} , components of the full spectrum $\sigma(E_{\text{ph}}|J_i = 0)$. In the parallel transition, both $\Omega_f = 0$ and $\Omega_f = 1$ states are initially populated in the A' symmetry states, but 86% of the population is in the $\Omega_f = 0$ block reached via the strongly angular dependent TDM μ_y . RT coupling is zero for $\Omega_f = 0$; it is active only in the almost empty $\Omega_f = 1$ block, reached via μ_z , and is promoted by the Coriolis-induced population transfer from $\Omega_f = 0$ to $\Omega_f = 1$. If the molecule dissociates exclusively out of $\Omega_f = 1$ states, Coriolis transitions control the dissociation rate. Dissociation of HCO in the \tilde{A}^2A'' state is a well known example.^{30,49} In contrast, dissociation of CO₂ is fast even for $\Omega_f = 0$ and the Coriolis interaction is inefficient on the characteristic time scale of $\tau_{\text{diss}} \sim \hbar/\bar{\Gamma}_n \sim 100$ fs. This is also the reason why CS approximation has little effect on the parallel spectrum σ_{\parallel} .

The perpendicular transition terminates in A'' states and is realized via TDM μ_x . The spectrum σ_{\perp} in Fig. 4(b) consists of two widely separated almost equally intense bands featuring apparently regular progressions of diffuse peaks. The reason for the distinct regularity of the 148 nm band in σ_{\perp} will be discussed in Sect. III C. The rotational state ($J_f = 1, \Omega_f = 1$) is exclusively populated, and the RT coupling is operative in the perpendicular transition. However, σ_{\perp} is substantially smaller than σ_{\parallel} for all but the highest photon energies: The TDM μ_x , which is similar to μ_z , depends weakly on α_{OCO} (see Fig. 3), and it is excitations from bent geometries which dominate the spectrum. As a result, the RT coupling, active in σ_{\perp} , has little influence on the sum $\sigma_{\perp} + \sigma_{\parallel}$.⁵⁰

The state $^1\Sigma_u^-$, decoupled from other states in this calculation, is excited in a perpendicular transition via μ_x . Its absorption spectrum, discussed in Sect. III D, consists of a series of sharp narrow lines, with the peak intensity reached in the gap between the two main bands. The TDM with \tilde{X} is extremely small in the FC region, and the absorption cross section does not exceed 5×10^{-20} cm². As a result, the contribution of the $^1\Sigma_u^-$ state is hardly discernible in the full spectrum. Test calculations register minor intensity gain if weak vibronic coupling to other states is included.

B. Vibronic assignments of the high energy band

The intense lines in the experimental 133 nm band [Fig. 1(b)] are spaced, on average, by $\sim 630 \text{ cm}^{-1}$. This major progression is shown by brown sticks in Fig. 4(a). Another progression can be recognized as minor peaks or shoulders above $72\,000 \text{ cm}^{-1}$. The minor peaks, also shown as sticks in Fig. 4(a), are red shifted by $\sim 250 \text{ cm}^{-1}$ with respect to the major ones. Above $77\,000 \text{ cm}^{-1}$, the diffuse bands consist of two clearly separated approximately equally intense peaks. Despite its simple appearance, even the major progression resists straightforward assignment because the spacings between the adjacent peaks are not constant. Instead, they obey an intricate rise-and-fall pattern in which intervals of frequency growth (for example, $73\,000 \text{ cm}^{-1}$ — $75\,000 \text{ cm}^{-1}$ or $76\,000 \text{ cm}^{-1}$ — $78\,000 \text{ cm}^{-1}$) are interrupted by dips (for example, near $73\,000 \text{ cm}^{-1}$, $75\,300 \text{ cm}^{-1}$, or $79\,000 \text{ cm}^{-1}$). Rablais et al. suggested that the progression is due to bending excitations in the near-linear molecule, with the perturbations originating from the Coriolis interaction between the vibrational and rotational angular momenta.¹⁵ The dynamics calculations suggest that the major progression is built on synchronized excitations of the two CO bonds.

In the calculated spectrum [Fig. 1(b) and 4(a)], the major and minor progressions are qualitatively similar to the experimental ones, but numerically different. For example, the spacings between major peaks follow the same rise-and-fall pattern, but their average is merely $\sim 580 \text{ cm}^{-1}$. Next, the minor progression, also seen in the calculations, is blue-shifted by $\sim 240 \text{ cm}^{-1}$ against the major one. Around $76\,000 \text{ cm}^{-1}$, the intensity of the minor peaks grows substantially and the calculated spectrum shows several strong lines giving it a congested appearance. Above $77\,000 \text{ cm}^{-1}$, most calculated peaks are split into two components in agreement with experiment. Thus, the achieved accuracy is not spectroscopic, but the calculated spectrum represents a reasonable starting point for the analysis of molecular motions behind the diffuse bands. The assignment, presented below, is based on the properties of metastable resonance states calculated specifically for the parallel component σ_{\parallel} of the full spectrum. The principal progressions are similar in $\sigma(E_{\text{ph}}|J_i = 0)$ and $\sigma_{\parallel}(E_{\text{ph}}|J_i = 0)$ [cf. Fig. 4(a) and (b)]. Differences visible above $78\,000 \text{ cm}^{-1}$ are addressed at the end of this section.

Positions, E_n , of resonance states excited in a parallel transition $(J_i = 0, \Omega_i = 0) \rightarrow (J_f = 1, \Omega_f = 0)$, calculated using filter diagonalization in the CS approximation, are illustrated

with sticks in Fig. 4(c). Each resonance is further characterized by its width Γ_n and the intensity $I_n = |\langle \Phi(J_i, \Omega_i) | \Psi_n \rangle|^2$. The resonance absorption spectrum,

$$\sigma_{\text{res}}(E_{\text{ph}} | J_f, \Omega_f) = \sum_n I_n \frac{\Gamma_n^2/4}{(E_{\text{ph}} - E_n)^2 + \Gamma_n^2/4}, \quad (16)$$

is compared with σ_{\parallel} in Fig. 4(c). Resonances are expected to accurately describe absorption spectra consisting of narrow isolated lines.⁵¹ However, despite a substantial fast direct contribution, the incoherent sum of Lorentzians in σ_{res} is in qualitative and — above 73 000 cm^{-1} — even in quantitative agreement with σ_{\parallel} , both in terms of positions of the diffuse lines and the intensity of the background.

Nodal patterns of resonance wave functions provide vibronic labels for the diffuse peaks. All resonances with $\Gamma_n \leq 150 \text{ cm}^{-1}$ were screened, but the discussion will be limited to states with the largest intensities. Their positions are shown with sticks in Fig. 4(d), and their widths range from 30 cm^{-1} to 80 cm^{-1} . Relevant for the assignment is the $3A'$ electronic component of the Ψ_n vector in the CI-adiabatic representation. Indeed, the 133 nm band is due to the linear adiabatic states $3^1A'/3^1A''$. Moreover, the considered parallel transition populates only A' states, with the population transfer into the A'' block suppressed for $\Omega_f = 0$ without Coriolis coupling. Direct dissociation in the state $3^1A'$ is hindered by a $\sim 1 \text{ eV}$ high barrier [see Fig. 1 of paper I], and the $3A'$ component of Ψ_n describes a vibrational level trapped in the upper adiabatic sheet of the cone and non-adiabatically coupled to the dissociation continuum of the lower $2A'$ sheet (cf. Ref. 52).

States in the major progression, which can be followed from the origin near 72 700 cm^{-1} up to at least 78 000 cm^{-1} , are illustrated in the left column of Fig. 5. The 3D wave functions are viewed in the (R_1, R_2) plane against the contour map of the $3A'$ potential containing the closed CI seam. Their assignment in terms of three quantum numbers (v_ϕ, v_r, v_b) is indicated above each frame and the respective combs are shown in Fig. 4(d). These quantum numbers reflect three features shared by the states in the main progression. First, they have no nodes along the bending direction except at $\alpha_{\text{OCO}} = 180^\circ$; most probable angles lie between 173° and 177° and the states are essentially ‘flat’, i.e. localized in the (R_1, R_2) plane. Such resonances are labelled by $v_b = 0$. Second, these states have no nodes along the direction normal to the CI seam, and their ‘radial’ quantum number is zero, $v_r = 0$. Third, these states describe consecutive excitations around the CI loop. In each successive state, two new nodes are ‘stringed’ on the CI seam ‘wire’, and the quantum number for this mode, v_ϕ ,

counts nodes along one side of the seam. All states in Fig. 5 are symmetric with respect to interchange of R_1 and R_2 , as expected for parallel transitions; antisymmetric states, with a node along the $R_1 = R_2$ line, remain ‘invisible’. The potential along the seam loop is rather smooth, and the average frequency in the v_ϕ progression is $\omega_\phi \sim 580 \text{ cm}^{-1}$. However, energies in the ‘angular’ v_ϕ progression are not equidistant (see below). The quantum numbers v_r and v_b correspond to the tuning and the coupling modes of the CI, respectively. The adiabatic potentials along these directions are cusped, and the vibrational frequencies ω_r and ω_b are expected to be much larger than ω_ϕ .

A simple two-dimensional (2D) reference model, which illustrates the impact of the closed CI seam on the eigenstates and the energy spectrum of the full Hamiltonian, consists of a single adiabatic $3^1A'$ PES in the (R_1, R_2) plane with fixed $\alpha_{\text{OCO}} = 179^\circ$. The 2D spectrum has been calculated using filter diagonalization, and examples of the 2D eigenstates are shown in the middle column of Fig. 5. They can be assigned two quantum numbers $(v_\phi, v_r)_{2\text{D}}$ measuring excitations along the angular seam mode ϕ and the radial stretching mode r . As in the full Hamiltonian, the states have either a maximum or a node along the line $R_1 = R_2$. Symmetric wave functions in the progression $(v_\phi, 0)_{2\text{D}}$ in Fig. 5 can be directly compared with states in the major progression $(v_\phi, 0, 0)$ in the left column. The 2D states are tightly localized around the CI loop, emphasizing that the quantum number v_ϕ describes hindered rotation in the (R_1, R_2) plane. Similarities in the wave functions are strong enough to make the 2D model useful in disentangling complicated nodal patterns in the full calculations. A good case in point is the progression $(v_\phi, 1)_{2\text{D}}$ built on one quantum of radial excitation and shown in the lower panels of Fig. 6. The frequency of the radial mode, $\omega_r = 2150 \text{ cm}^{-1}$, is almost four times the hindered rotation frequency. Resonance anharmonic couplings mix the states $(v_\phi, 0)_{2\text{D}}$ and $(v_\phi - 4, 1)_{2\text{D}}$, but their wave functions remain clearly recognizable in 2D (compare states marked with stars in Fig. 5 and 6). The progression of states with $v_r = 1$ is found in the full calculation, too (Fig. 6, upper panels). The fundamental radial frequency, $\omega_r = 1560 \text{ cm}^{-1}$, is lower than in 2D. Nevertheless, the anharmonicity is strong and many states $(v_\phi, 0, 0)$ and $(v_\phi - 4, 1, 0)$ are mixed making their assignment difficult. In fact, the states in the upper panels of Fig. 6 were identified using their 2D analogues. Moreover, most states $(v_\phi, 1, 0)$ are discernible merely as satellites to the major peaks $(v_\phi, 0, 0)$; their intensity increases only above $78\,000 \text{ cm}^{-1}$ [see Fig. 4(d)]. As a result, many members of this progression are missing, but the gaps can be filled in by the 2D model (cf. Fig. 6).

The third progression clearly visible in the calculated spectrum consists of resonances with a node at a bending angle $\alpha_{\text{OCO}} < 180^\circ$. Such states are assigned $(v_\phi, v_r, 1)$. The state $(0, 0, 1)$ lies at $75\,300\text{ cm}^{-1}$, so that the bending frequency is $\omega_b = 2290\text{ cm}^{-1}$. The intensity in this progression quickly grows with energy. Of the three strong bands, ‘congesting’ the spectrum between $75\,000\text{ cm}^{-1}$ and $76\,000\text{ cm}^{-1}$, two are due to states $(2, 0, 1)$ and $(3, 0, 1)$; only one state, $(6, 0, 0)$, has no bending excitation. Above $76\,000\text{ cm}^{-1}$ the states $(v_\phi, 0, 1)$ have the largest intensities. Their wave functions, shown in the right column of Fig. 5, are similar to the respective states with $v_b = 0$ and can again be analyzed in the (R_1, R_2) plane. Bending excitation introduces an additional ‘layer’ of nodes and enhances mixing between the combination states $(v_\phi, 0, 1)$ and $(v_\phi - 4, 1, 1)$ and both assignments are given in some panels. Above $78\,000\text{ cm}^{-1}$, the assignments become even less unique. Several factors contribute: Resonances substantially broaden, states with $v_b > 1$ are found, and mixing among the three vibrational motions increases. Conservative assignment associates the simple looking high energy bands with progressions $(v_\phi, 0, 1)/(v_\phi - 4, 1, 1)$ and $(v_\phi, 1, 0)$, although this selection is by no means unique.

The shape of the lower adiabatic potential in the plane of the tuning and the coupling modes of a CI is often referred to as a Mexican hat, especially in the context of the $E \times \epsilon$ Jahn-Teller effect.³³ A closed CI seam discussed in this paper adds another hat to the rack: A ‘Mongolian hat’, sketched in Fig. 5, is a piece of headwear which describes best the shape of the upper adiabatic PES in the (R_1, R_2) plane containing the CI seam. The hindered rotation excitations are winding along the hat brim (the CI seam), while consecutive radial excitations extend towards (and eventually engulf) the top of the hat.

The closed CI seam leaves a clear mark in the calculated absorption spectrum. Frequencies in the progression of pure v_ϕ excitations are shown in Fig. 7, in panel (b) for the full calculation and in panel (c) for the 2D model. Consider the model first. Energy intervals grow between $E_{\text{ph}} = 73\,000\text{ cm}^{-1}$ and $76\,000\text{ cm}^{-1}$, and this is consistent with a pseudorotational motion around the seam and the associated quantization with $E_\phi \sim v_\phi^2$. At the same time, the frequency in the $(v_\phi, 0)_{2\text{D}}$ progression is not monotonic, and there are two dips at low and high energies. Minimum in a progression frequency is often an indication that a critical energy in the potential (a barrier top or a saddle)⁵³ or in the phase space (a separatrix) has been reached.^{54,55} Possible sources of the rise-and-fall pattern in the 2D model are illustrated in the lower panels of Fig. 7 showing one-dimensional cuts through

the PES of the adiabatic $3^1A'$ state, taken along the seam [panel (d)] and across the seam [panel (e)]. Angular coordinate ϕ along the seam in (d) is chosen such that $\phi = 180^\circ$ for $R_1 = R_2 = 2.24 a_0$; the ‘radial’ coordinate in (e) runs along the antisymmetric stretch R_- , and the origin $R_- = 0$ is the point $R_1 = R_2 = 2.5 a_0$. The potential along the seam has two global minima separated by a local one at $\phi = 180^\circ$. The first frequency dip (gray color) in the $(v_\phi, 0)_{2D}$ progression involves the excited state in the global well and the ground state in the local well. The second frequency dip (yellow color) involves the states located near two types of critical points: The barriers, separating the local and the global minima along the seam [$\phi = 135^\circ$ and 225° in panel (d)], and the top of the Mongolian hat, separating the global minima across the seam [$R_- = 0$ in panel (e)].

The principal topographic features, captured by the 2D model, shape the spectrum in the full calculation, too. The frequency in progression $(v_\phi, 0, 0)$ in Fig. 7(b), although numerically different from the 2D case, grows steadily up to $E_{\text{ph}} \approx 75\,000 \text{ cm}^{-1}$ reflecting consecutive pseudorotational excitations along the CI seam. The frequency dip at high energies indicates that the top of the Mongolian hat has been reached, while the low energy dip is absent because the origin of the progression lies above the bottom of the local minimum at $\phi = 180^\circ$.

The accuracy of the ab initio PESs does not allow a line by line comparison with the measured spectrum. To which extent the above assignment is applicable to the experiment? Energy intervals in the major progression measured below $E_{\text{ph}} = 78\,000 \text{ cm}^{-1}$ are shown in Fig. 7(a), and the rise-and-fall pattern, inherent to the calculated spectra, appears to be distinctly recognizable, including a stretch of pseudorotational excitations and dips implying potential saddles. This observation should not be overinterpreted — shown is one progression, and this progression is rather short. If, however, the agreement with the calculations is more than a mere coincidence, the 133 nm band would be the first documented spectroscopic observation of a closed CI seam.

I would like to conclude the discussion of the 133 nm band by pointing out an alternative explanation for the double peaked lines above $78\,000 \text{ cm}^{-1}$. Their assignment in terms of progressions $(v_\phi, 0, 1)$ and $(v_\phi, 1, 0)$ has been given only for the parallel component of the total spectrum. Decomposition into σ_{\parallel} and σ_{\perp} at the bottom of Fig. 4(b) demonstrates that intensities in the two transitions become comparable at high photon energies. In fact, each double peaked line in the total spectrum consists of a low energy parallel peak (green line) overlapped with a high energy perpendicular peak (red line).

C. Vibronic assignments of the low energy band

Assignment of the 148 nm band is a challenging problem: Diffuse structures are weak, irregular, and overlapping. Substantial bending excitation has been suggested for this band^{17,26} originating from states $2^1A'$ and $1^1A''$ with strongly bent equilibrium geometries.^{22,26} The present calculations demonstrate that actual molecular motion is difficult to define in terms of the familiar normal modes: Energy above equilibrium is high and the anharmonic and vibronic couplings are substantial. The results summarized in this section at best provide an initial point from which a genuine analysis could be undertaken.

In the experimental spectrum, almost every diffuse structure below $72\,000\text{ cm}^{-1}$ comprises several transitions visible as a group of peaks or as a shoulder [Fig. 1(b)]. Diffuse structures in the calculated spectrum look similar, especially after thermal averaging, although irregularities in the energy intervals, widths, and intensities preclude a meaningful matching with experiment. In order to enable comparison, line subsets are selected in both spectra. In the experimental spectrum, centers of the diffuse peaks with the largest intensities are chosen as indicated in Fig. 4(a). In the calculated spectrum, only the parallel transition ($J_i = 0, \Omega_i = 0$) \rightarrow ($J_f = 1, \Omega_f = 0$) is initially considered, and resonance states Ψ_n with the largest intensities are taken to represent diffuse peaks in σ_{\parallel} [Fig. 4(d)].

Energy intervals between the selected peaks are shown in Fig. 8 ($E_{\text{ph}} \geq 60\,000\text{ cm}^{-1}$). Experimental peaks are spaced by 400 cm^{-1} — 700 cm^{-1} . Spacings between the intense resonances vary in similar limits although the agreement is only qualitative. Moreover, visual assignment of the wave functions fails for the selected resonances. A typical example is given in Fig. 9 which depicts the $2A'$ adiabatic component of a state lying at $E_{\text{ph}} = 8.38\text{ eV}$, i.e. $\sim 3\text{ eV}$ above equilibrium of the $2A'$ state and $\sim 1\text{ eV}$ above dissociation threshold. The large excess energy is the reason for the bizzar nodal patterns of the $2A'$ resonance components, and — although wave functions of different states in Fig. 4(d) have different nodal patterns — their complexity is beyond rationalization in terms of progressions.

An alternative ‘bottom-up’ approach in this case is to study the spectrum of the bent $2^1A'$ state from the ground state upwards and to follow the characteristic frequencies with growing internal energy. Bent electronic states have C_{2v} equilibria (see Table III of paper I), and the relevant vibrational quantum numbers are the symmetric stretch v_s , the bend v_b , and the antisymmetric stretch v_a . All wave functions in the full calculations, both resonance and

bound, were screened in order to find states, $2A'$ adiabatic components of which represent pure excitations in the three vibrational modes. Examples of pure stretching and bending wave functions are shown in Figs. 10 and 11, respectively. The progression $(v_s, 0, 0)$ is the simplest: Consecutive wave functions have parallel nodal lines (normal to which indicates the normal mode direction), and the symmetric stretch frequency $\omega_s \approx 1400 \text{ cm}^{-1}$ is mildly anharmonic and depends smoothly on energy (see Fig. 8, $E_{\text{ph}} < 60\,000 \text{ cm}^{-1}$). In the progression $(0, 0, v_a)$, only states with even v_a are visible, because the transition is parallel and both μ_y and μ_z are symmetric with respect to interchange of R_1 and R_2 . The antisymmetric stretch frequency, $\omega_a \approx 900 \text{ cm}^{-1}$, grows at low energies, passes through a maximum near $49\,000 \text{ cm}^{-1}$ and then decreases (Fig. 8); nodal lines in the lower panels of Fig. 10 noticeably bend in the (R_1, R_2) plane with growing v_a . The anharmonicity is the strongest in the bending progression $(0, v_b, 0)$. While the direction of the bending vibration is rather well preserved, its frequency in Fig. 8 varies from $\omega_b(A') \approx 550 \text{ cm}^{-1}$ down to 380 cm^{-1} , experiencing a slow rise followed by a rapid decline above $49\,000 \text{ cm}^{-1}$. The mode coupling and the density of states grow substantially above $E_{\text{ph}} = 52\,000 \text{ cm}^{-1}$, rendering further search for pure excitations unfeasible. This leaves a $10\,000 \text{ cm}^{-1}$ wide energy gap between the last assigned state and the resolvable red edge of the 148 nm band. In view of the capricious anharmonicities, an extrapolation over this gap would seem unreliable for any mode but the symmetric stretch. However, if it is granted that the two lowest frequencies, $\omega_b \sim 350 \text{ cm}^{-1}$ and $\omega_a < 900 \text{ cm}^{-1}$, keep their values up to and above $60\,000 \text{ cm}^{-1}$, one would expect the diffuse peaks to reflect strongly excited bending and antisymmetric stretch motions.

One major drawback of the above discussion is the missing experimental counterparts of the calculated vibrational frequencies: The measured intensities are low and the rotational structure is unresolved. Truly exceptional in this respect is the high resolution study of the wavelength range 172 nm — 198 nm , performed by Cossart-Magos and co-workers¹⁹ who were able to detect many absorption bands with rotational structure and to isolate two vibrational progressions between $51\,000 \text{ cm}^{-1}$ and $57\,000 \text{ cm}^{-1}$. This energy range overlaps with the energies in which pure excitations in the quantum mechanical calculations still could be detected. The progressions were assigned to the electronic state 1^1A_2 , i.e. the bent state $1^1A''$, excited in a perpendicular transition from \tilde{X} . Frequencies in the experimental progressions are shown with open triangles and squares in Fig. 8; open circles are the frequency shifts between states belonging different progressions. In Ref. 19, both progressions were

interpreted as consecutive bending excitations differing by one quantum of the symmetric stretch, giving experimental estimates of $\omega_b \approx 600 \text{ cm}^{-1}$ and $\omega_s \approx 1370 \text{ cm}^{-1}$. Relevant theoretical progressions are shown in Fig. 8 with red symbols. They are obtained by calculating eigenstates in the perpendicular transition $(J_i = 0, \Omega_i = 0) \rightarrow (J_f = 1, \Omega_f = 1)$ in many energy windows and looking for the wave functions $\Psi_n, 1A''$ adiabatic components of which represent consecutive bending excitations. Because $\mu_x(R_1, R_2) = -\mu_x(R_2, R_1)$, all excited states involve odd number of quanta in the antisymmetric stretching mode v_a . The progression shown in the lower part of Fig. 8 (red squares) is $(1, v_b, 1)$, and the frequency shifts with respect to the progression $(0, v_b, 1)$ are given in the upper part of Fig. 8 (red circles). The calculation clearly confirms the experimental assignment. Agreement with the experiment is quantitative, especially for the bending frequency $\omega_b(A'')$ in the $(1, v_b, 1)$ progression, which lies within 10 cm^{-1} of the experimental values. Somewhat less accurate is the symmetric stretch frequency shift and its energy variation. Most probably, this implies that the observed progressions are built on higher symmetric stretch excitations than $v_s = 0$ and $v_s = 1$. The calculated intensity generally grows with v_s , but sufficiently long bending progressions with $v_s \geq 2$ become tough to identify.

The bending progressions in the parallel and perpendicular transitions shown in in Fig. 8 are strikingly different: $\omega_b(A'')$ in σ_\perp smoothly depends on energy and is only slightly anharmonic, while $\omega_b(A')$ in σ_\parallel has a strong non-monotonic energy dependence. This is surprising because the equilibria of the bent states $2^1A'$ and $1^1A''$ are similar. The sole difference is in the equilibrium angle, 127° in $1^1A''$ vs. 118° in $2^1A'$, but it can hardly be made responsible for the observed discrepancy in the bending frequencies. Instead, the strong energy dependence of $\omega_b(A')$ stems from another property of the $2^1A'$ PES along the bending angle: In the calculation, it is this state to which the carbene-type bent OCO minimum at 70° belongs after local diabatization of bent CIs. This minimum at $\alpha_{\text{OCO}} = 73^\circ$ is clearly seen in the contour maps in Fig. 11. Near $E_{\text{ph}} \approx 48\,000 \text{ cm}^{-1}$, the ground vibrational state appears in this local OCO minimum shown in the left lower panel in Fig. 11. Above $50\,000 \text{ cm}^{-1}$, the bending states in the local and in the global equilibria become connected via a saddle point, the main bending progression includes states partially delocalized between the two wells [right lower panel in Fig. 11], the configuration space available to bending vibrations suddenly expands, and it is this energy range in which $\omega_b(A')$ starts to decrease. In contrast, the $1^1A''$ state, diabatized at bent CIs in a different symmetry block, loses the

OCO bent minimum which becomes reassigned to state $3^1A''$. As a consequence, the energy dependence of $\omega_b(A'')$ is monotonic and inconspicuous.

The difference in bending progressions in the states $2^1A'$ and $1^1A''$ and its connection to the local OCO minimum along α_{OCO} allows one to explain the difference in the diffuse structures in the parallel and perpendicular excitations of the 148 nm band in Fig. 4(b). A nearly constant frequency $\omega_b(A'')$ correlates with the regular progression of peaks in σ_{\perp} . On the other hand, the bending frequency $\omega_b(A')$ in the parallel excitation is small and strongly energy dependent — and the diffuse peaks in σ_{\parallel} are narrowly spaced, irregular, and overlapping. Simultaneous analysis of both types of transitions indirectly confirms that the observed absorption lines are indeed due to strong bending excitations: Qualitatively different bending potentials support qualitatively different spectra. Moreover, the ‘congestion’ in the 148 nm parallel band is interpreted as a direct consequence of the carbene-type OCO ‘cyclic’ minimum in the bent $2^1A'$ state.

It is worth reminding the reader that the question of electronic assignment of the carbene-type OCO goes beyond the diabatic states $2^1A'$, $1^1A''$, or the ground electronic state in which it was discovered by Xantheas and Ruedenberg.⁵⁶ In paper I, the origin of this minimum was traced to the states $4^1A'$ and $4^1A''$ correlating at linearity with the Rydberg state $2^1\Delta_u$. The influence of the carbene-type OCO on the diffuse 148 nm band, uncovered in the above calculations, suggests that a systematic analysis of this band has to include the first four A' and A'' states properly diabaticized and fully interacting at multiple bent CIs.

D. Vibrational assignments in the state $^1\Sigma_u^-$

The spectrum of the state $2^1A''$ ($^1\Sigma_u^-$ at linearity) is shown in Fig. 12. It stretches from $65\,000\text{ cm}^{-1}$ to about $83\,000\text{ cm}^{-1}$ and consists of several series of narrow peaks. All vibrational states, excited in this transition, lie below $92\,430\text{ cm}^{-1}$, i.e. the threshold energy of the channel $\text{O}(^3P) + \text{CO}(a^3\Pi)$ with which the state $^1\Sigma_u^-$ correlates. Predissociation is purely non-adiabatic and therefore inhibited in these calculations. Because of the extremely small TDM μ_x , the intensity of this band, excited in a perpendicular transition from \tilde{X} , does not exceed $6 \times 10^{-20}\text{ cm}^{-2}$. The frequencies of the bending, symmetric and antisymmetric stretching modes are $\omega_b = 576.7\text{ cm}^{-1}$, $\omega_s = 1015.5\text{ cm}^{-1}$, and $\omega_a = 1118.7\text{ cm}^{-1}$, respectively. The vibrational ground state $(0, 0, 0)$ lies at 64220 cm^{-1} but remains invisible in a

perpendicular transition in which only states with odd number of antisymmetric stretch quanta v_a are excited. Most intense lines in the spectrum belong to one of the three main progressions, assigned by visual inspection of the corresponding wave functions, although excitations are easily predictable from the FC geometries. The state ${}^1\Sigma_u^-$ is linear, the angular dependence of the TDM μ_x is weak, and the bending vibration remains unexcited. In contrast, the equilibrium bond lengths, $R_1 = R_2 = 2.4 a_0$, are substantially extended as compared to the equilibrium in \tilde{X} at $R_1 = R_2 = 2.20 a_0$, with the implication that the spectrum is built on stretching excitations. The nodal patterns of the vibrational eigenfunctions clearly demonstrate that the three main progressions, $(v_s, 0, 1)$, $(v_s, 0, 3)$, and $(v_s, 0, 5)$, involve consecutive excitations of the symmetric stretch mode accompanied by one, three, or five quanta of the antisymmetric stretch. Maximum intensity in each progression is reached for the same $v_s = 7$, and the intensity distributions around the maximum are approximately bell shaped.

IV. SUMMARY AND CONCLUDING REMARKS

This paper analyzes the absorption spectrum of carbon dioxide in the wavelength range 120 nm — 160 nm by means of quantum mechanical calculations using PESs of five singlet valence electronic states and their coordinate dependent TDM vectors with the ground electronic state, constructed as described in paper I. The main results are as follows:

1. The UV spectrum of five valence states, calculated for $T = 190$ K via Boltzmann averaging of optical transitions from many initial rotational states, reproduces the experimental two-band spectral envelope, the positions of the absorption maxima, their FWHMs, peak intensities, and frequencies of diffuse structures in each band.
2. The two absorption bands have been assigned at several levels of graining. Electronic assignment, reflecting the strong HT effect and influenced by the vibronic interactions at CIs, is given in the adiabatic representation (low energy band: bent states $2{}^1A'/1{}^1A''$; high energy band: linear states $3{}^1A'/3{}^1A''$; gap between the two bands: state $2{}^1A''$). The parallel and perpendicular components of the full spectrum are isolated. The parallel transition, the RT coupling in which is suppressed for excitations from the ground vibrational state in \tilde{X} , is shown to be dominant for all but the highest photon

energies. Finally, individual diffuse structures are assigned using multicomponent wave functions of metastable resonance states.

3. *In the high energy band*, the main progressions correspond to consecutive excitations of the pseudorotational motion around the closed loop of the CI seam; progressions differ in the number of nodes along the radial mode perpendicular to the closed seam. Systematic frequency growth in the pseudorotational progressions is interpreted as a spectroscopic hallmark of the closed seam.
4. *In the low energy band*, the diffuse peaks, associated with bending excitations in the states $2^1A'$ and $1^1A''$, are analyzed in both parallel and perpendicular transitions. Calculations reveal a dramatic difference in the spectra of the two states. The perpendicular band (mainly $1^1A''$), bending progressions in which are nearly equidistant, is rather regular. In contrast, bending excitations in the parallel band (mainly $2^1A'$), are very anharmonic and irregular. This difference is interpreted as a manifestation of the carbene-type ‘cyclic’ OCO minimum in the PES of the $2^1A'$ state.

The present study focuses on spectroscopic aspects of the UV photodynamics of CO_2 . Mechanisms of photodissociation are discussed only insofar as they become apparent in the analysis of the absorption spectrum. This piece will be completed in the discussion of photofragment distributions which will be published separately. However, preliminary conclusions can be deduced from the density distributions of resonance wave functions Ψ_n calculated and discussed above. Of interest here are the $2A'$ components of Ψ_n as depicted for example in Fig. 9. Although useless in establishing the vibrational assignments, they rather clearly illustrate the dissociation path taken by the molecule once it arrives in a bent adiabatic state. Because of CIs in linear CO_2 , the inner regions of states $2^1A'$ and $1^1A''$ are separated from the dissociation asymptotes by barriers. On the other hand, the $2^1A'$ and $1^1A''$ potentials along α_{OCO} in the direction of global bent equilibria are barrierless. This directional anisotropy is reflected in the probability density in the right panel of Fig. 9: The wave function traces out a path leading from the FC region to smaller angles; hardly any probability is found along the linear dissociation path. Substantial extension of the CO bond, seen in the left panel of Fig. 9, occurs predominantly in bent molecular configurations with $\alpha_{\text{OCO}} < 140^\circ$. This shape is representative of the $2A'$ or $1A''$ components of Ψ_n both

below the CI energy (where the bent states are directly accessed) and above the CI energy (where they become populated indirectly via the CI funnels at linearity).

Acknowledgments

Financial support by the Deutsche Forschungsgemeinschaft is gratefully acknowledged

-
- ¹ S. Yu. Grebenshchikov, *J. Chem. Phys.* **137**, 021101 (2012).
- ² S. Yu. Grebenshchikov, preceding paper .
- ³ Up-to-date atmospheric CO₂ concentrations can be found at [<http://www.esrl.noaa.gov/gmd/ccgg/trends>].
- ⁴ *UNFCCC, The Cancun Agreements, FCCC/CP/2010/7/Add.1 (United Nations Framework Convention on Climate Change, 2010)*.
- ⁵ T. F. Stocker, *Science* **339**, 280 (2013).
- ⁶ A. J. Traynor and R. J. Jensen, *Ind. Eng. Chem. Res.* **41**, 1935 (2002).
- ⁷ S. C. Roy, O. K. Varghese, M. Paulose and C. A. Grimes, *ACSNano* **4**, 1259 (2010).
- ⁸ P. D. Feldman, E. B. Burgh, S. T. Durrance and A. F. Davidsen, *Astrophys. J.* **538**, 395 (2000).
- ⁹ V. Vuitton, R. V. Yelle and J. Cui, *J. Geophys. Res. (Planets)* **113**, 5007 (2008).
- ¹⁰ W. D. Geppert, C. Naulin and M. Costes, *Chem. Phys. Lett.* **364**, 121 (2002).
- ¹¹ T. Lyman, *Astrophys. J.* **27**, 87 (1908).
- ¹² E. C. Y. Inn, K. Watanabe and M. Zelikoff, *J. Chem. Phys.* **21**, 1648 (1953).
- ¹³ G. Herzberg. *Molecular Spectra and Molecular Structure III. Electronic Spectra and Electronic Structure of Polyatomic Molecules*. Van Nostrand, Princeton, (1967).
- ¹⁴ M. Ogawa, *J. Chem. Phys.* **54**, 2550 (1971).
- ¹⁵ J. W. Rabalais, J. M. McDonald, V. Scherr and S. P. McGlynn, *Chem. Rev.* **71**, 73 (1971).
- ¹⁶ W. F. Chan, G. Cooper and C. E. Brion, *Chem. Phys.* **178**, 401 (1993).
- ¹⁷ K. Yoshino, J. R. Esmond, Y. Sun, W. H. Parkinson, K. Ito and T. Matsui, *J. Quant. Spect. Radiat. Transf.* **55**, 53 (1996).
- ¹⁸ G. Stark, K. Yoshino, P. L. Smith and K. Ito, *J. Quant. Spect. Radiat. Transf.* **103**, 67 (2007).
- ¹⁹ C. Cossart-Magos, F. Launay and J. E. Parkin, *Mol. Phys.* **75**, 835 (1992).
- ²⁰ C. Cossart-Magos, F. Launay and J. E. Parkin, *Mol. Phys.* **103**, 629 (2005).
- ²¹ C. Cossart-Magos, M. Jungen and F. Launay, *Mol. Phys.* **61**, 1077 (1987).
- ²² R. N. Dixon, *Proc. Roy. Soc. A* **275**, 431 (1963).
- ²³ W. B. England and W. C. Ermler, *J. Chem. Phys.* **70**, 1711 (1979).
- ²⁴ P. J. Knowles, P. Rosmus and H.-J. Werner, *Chem. Phys. Lett.* **146**, 230 (1988).
- ²⁵ A. Spielfiedel, N. Feautrier, G. Chambaud, P. Rosmus and H.-J. Werner, *Chem. Phys. Lett.*

- 183**, 16 (1991).
- ²⁶ A. Spielfiedel, N. Feautrier, C. Cossart-Magos, G. Chambaud, P. Rosmus, H.-J. Werner and P. Botschwina, *J. Chem. Phys.* **97**, 8382 (1992).
- ²⁷ Wave packet calculations of Light and Kulander [*J. Chem. Phys.*, **73**, 4337 (1980)] simulated UV absorption of CO₂ using a two-dimensional model LEPS potential. The diffuse structures in the calculated spectrum were related to several distinct types of unstable periodic orbits describing the symmetric stretch excitations and combinations of the symmetric and antisymmetric stretch [see, for example, R. Schinke, 'Photodissociation dynamics', Cambridge University Press, Cambridge (1993)]. These calculations shaped our present understanding of quantum-classical correspondence in the photodissociation of small polyatomic molecules. At the same time, the unrealistic LEPS potential makes it difficult to relate this model to any particular electronic transition in CO₂.
- ²⁸ R. Renner, *Z. Phys.* **92**, 172 (1934).
- ²⁹ C. Petrongolo, *J. Chem. Phys.* **89**, 1297 (1988).
- ³⁰ E. M. Goldfield, S. K. Gray and L. B. Harding, *J. Chem. Phys.* **99**, 5812 (1993).
- ³¹ S. Yu. Grebenshchikov and R. Borrelli, *J. Phys. Chem. Lett.* **3**, 3223 (2012).
- ³² Ab initio calculations in paper I use a different coordinate system (x' , y' , z'): x' is orthogonal to the molecular plane, z' runs along one of the CO bonds and $y' \perp z'$. It is related to the principal axes system by an orthogonal transformation.
- ³³ H. Köppel, W. Domcke and L. S. Cederbaum, *Adv. Chem. Phys.* **57**, 59 (1984).
- ³⁴ D. J. Tanor, *J. Phys. Chem.* **92**, 3341 (1988).
- ³⁵ G. Orlandi and W. Siebrand, *J. Chem. Phys.* **58**, 4513 (1973).
- ³⁶ J.Z.H. Zhang. *Theory and Application of Quantum Molecular Dynamics*. World Scientific, Singapore, (1999).
- ³⁷ J. Tennyson and B. T. Sutcliffe, *J. Chem. Phys.* **77**, 4061 (1982).
- ³⁸ G. G. Balint-Kurti, *Adv. Chem. Phys.* **128**, 249 (2004).
- ³⁹ V. A. Mandelshtam and H. S. Taylor, *J. Chem. Soc. Faraday Trans.* **93**, 847 (1997).
- ⁴⁰ G. Jolicard and E. J. Austin, *Chem. Phys. Lett.* **121**, 106 (1985).
- ⁴¹ H. Tal-Ezer and R. Kosloff, *J. Chem. Phys.* **81**, 3967 (1984).
- ⁴² V. A. Mandelshtam and H. S. Taylor, *J. Chem. Phys.* **103**, 2903 (1995).
- ⁴³ M. R. Wall and D. Neuhauser, *J. Chem. Phys.* **102**, 8011 (1995).

- ⁴⁴ J. C. Light and T. Carrington, *Adv. Chem. Phys.* **114**, 263 (2000).
- ⁴⁵ J. Echave and D. C. Clary, *Chem. Phys. Lett.* **190**, 225 (1992).
- ⁴⁶ B. Kirmse, B. Abel, D. Schwarze, S. Yu. Grebenshchikov and R. Schinke, *J. Phys. Chem. A* **104** (2000).
- ⁴⁷ ‘PolyWave’ is a package of FORTRAN90 programs for iterative quantum mechanical calculations of bound states, dissociative resonance states, photoabsorption or photoemission spectra, as well as product state distributions in molecules with up to six internal degrees of freedom and $N \leq 9$ coupled electronic states. The package is available from the author upon request.
- ⁴⁸ S. Yu. Grebenshchikov, R. Schinke, Z.-W. Qu and H. Zhu, *J. Chem. Phys.* **124**, 204313 (2006).
- ⁴⁹ J. Weiß, R. Schinke and V. A. Mandelshtam, *J. Chem. Phys.* **113**, 4588 (2000).
- ⁵⁰ TDM μ_x depends linearly on the antisymmetric stretch coordinate R_- , with the effect that a node is created in the initial excitation prepared in a perpendicular transition. This is illustrated in Fig. 2(b), which shows that the initial wave packet $\sim \mu_x \psi_0^{1,0}$ has two maxima near $R_1 = 2.1 a_0$ and $R_1 = 2.3 a_0$. These maxima are reflected in the wide separation of the two bands in σ_\perp [see, for example, R. Schinke, ‘Photodissociation dynamics’, Cambridge University Press, Cambridge (1993)].
- ⁵¹ S.Yu. Grebenshchikov, R. Schinke and W. L. Hase. In *Unimolecular Kinetics*, edited by N. Green. (Elsevier, Amsterdam, 2003).
- ⁵² J. C. Slonczewski, *Phys. Rev. Lett.* **131**, 1596 (1963).
- ⁵³ J. R. Cary, P. Rusu and R. T. Skodje, *Phys. Rev. Lett.* **58**, 292 (1987).
- ⁵⁴ M. E. Kellman, *Annu. Rev. Phys. Chem.* **46**, 395 (1995).
- ⁵⁵ J. Weiss, J. Hauschildt, S.Yu. Grebenshchikov, R. Düren, R. Schinke, J. Koput, S. Stamatiadis and S. C. Farantos, *J. Chem. Phys.* **112**, 77 (2000).
- ⁵⁶ S. S. Xantheas and K. Ruedenberg, *Int. J. Quant. Chem.* **49**, 409 (1994).

FIG. 1: (a) Experimental absorption cross section of CO_2 ($T = 195 \text{ K}$; in cm^2) as a function of photon energy (in 10^3 cm^{-1}). Numbers on the cross section axis denote powers of ten. The photon energy range studied in this work is indicated with two dashed lines. (b) Absorption spectrum, calculated at $T = 200 \text{ K}$ (blue line, vertically shifted by $0.9 \cdot 10^{-18} \text{ cm}^2$), compared with the experimental spectrum (black line). Electronic assignment in terms of adiabatic states is given. Experimental data are from Ref. 17. Theoretical spectrum is shifted by 400 cm^{-1} to lower energies.

FIG. 2: Cuts through the PESs of the adiabatic states along (a) OCO angle (fixed coordinates are $R_1 = 2.2 a_0$ and $R_2 = 2.3 a_0$) and (b) one CO bond distance (fixed coordinates are $R_{\text{CO}} = 2.3 a_0$ and $\alpha_{\text{OCO}} = 175^\circ$). The thick black line in both panels is the ground electronic state \tilde{X} ; excited A' and A'' states are shown with thin black and brown lines, respectively. Red lines and arrows illustrate the non-vertical excitation process and the effect of the TDM on the initial vibrational wave function ψ_0 in \tilde{X} . ψ_0 is shown in both panels with a dashed line, and the shapes of the initial state in the optical transitions via y and x components of the TDM, $\mu_y \psi_0$ (a) and $\mu_x \psi_0$ (b) are shown with solid lines. Arrows, indicating excitations, pass through the maximum of ψ_0 and the maxima of $\mu_y \psi_0$ and $\mu_x \psi_0$.

FIG. 3: Spatial components μ_x (a,d), μ_y (b,e), and μ_z (c,f) of the ab initio TDM vectors for the adiabatic states $2^1A'$ (purple), $3^1A'$ (brown), $1^1A''$ (black), $2^1A''$ (purple), and $3^1A''$ (brown) from the ground state \tilde{X}^1A' . A' states are shown with solid, A'' states with open symbols. Dependences on the CO bond distance are shown in (a)—(c) [fixed coordinates are $R_2 = 2.2 a_0$ and $\alpha_{\text{OCO}} = 179^\circ$] and dependences on the OCO angle are shown in (d)—(f) [fixed coordinates are $R_1 = 2.2 a_0$ and $R_2 = 2.3 a_0$]. TDMs are measured in atomic units. The coordinate axes are sketched in (b): y is directed along the molecular figure axis, and z is normal to y in the molecular plane, and x is normal to the molecular plane.

FIG. 4: (a) The absorption spectrum $\sigma(E_{\text{ph}}|J_i = 0)$ for a single initial state $J_i = 0$ (blue) compared with the spectrum of Ref. 17 measured at $T = 195$ K (black). Thin sticks indicate the major experimental peaks separated into a strong (brown) and a weak (blue) progression in the high energy band, and a strong progression in the low energy band (black). Their positions are taken from Table X of Ref. 15 augmented with data from Ref. 17. Panels (b-d) show decomposition of the calculated spectrum and vibronic assignments: (b) $\sigma(E_{\text{ph}}|J_i = 0)$ spectrum (thin gray line) broken down into two low resolution components stemming from excitations of the bent ($2^1A'$, $1^1A''$, thick black line) and linear ($3^1A'$, $3^1A''$, thick blue line) adiabatic states. Two spectra at the bottom are the parallel (σ_{\parallel} , thick green line) and the perpendicular (σ_{\perp} , thick red line) components of $\sigma(E_{\text{ph}}|J_i = 0)$; (c) Decomposition of σ_{\parallel} (green) in terms of resonance states of the Hamiltonian Eq. (11). Gray sticks mark resonance positions (every 3d calculated state is shown). Black line is the sum of Lorentzians in Eq. (16); (d) Vibronic assignment of σ_{\parallel} (green) in terms of the most intense resonances shown at the bottom of the panel with thin sticks. Vertical shift of the calculated spectra is $0.9 \cdot 10^{-18} \text{ cm}^2$ in panels (a) and (b), and $0.6 \cdot 10^{-18} \text{ cm}^2$ in panels (c) and (d).

FIG. 5: *Left and right columns* depict $3A'$ adiabatic components of the 3D wave functions of resonance states in progressions $(v_{\phi}, 0, 0)$ and $(v_{\phi}, 0, 1)$, respectively. Shown in molecular coordinates is one particular contour $|\Psi(R_1, R_2, \alpha_{\text{OCO}})|^2 = \text{const.}$ The contour is viewed along the α_{OCO} axis and appears ‘projected’ onto the (R_1, R_2) plane. Shading emphasizes the 3D character of the plots. *Middle column* depicts contour maps of the eigenstates $\psi_{2\text{D}}(R_1, R_2)$ calculated in the 2D single state model. All states belong to progression $(v_{\phi}, 0)_{2\text{D}}$; red contours represent positive, blue contours negative values of $\psi_{2\text{D}}$. In all panels, a 2D contour map of the $3A'$ adiabatic potential for $\alpha_{\text{OCO}} = 179^\circ$ (gray lines) and the CI seam (black thick line) are sketched. Axis tic labels are in a_0 . States marked $(v_{\phi}, 0)_{2\text{D}}^*$ are mixed with states $(v_{\phi} - 4, 1)_{2\text{D}}^*$ shown in Fig. 6. The top middle panel shows author’s drawing of a Mongolian hat.

FIG. 6: *Upper panels:* $3A'$ adiabatic components of the 3D wave functions of resonance states in the progression $(v_{\phi}, 1, 0)$. The state $(3, 1, 0)$ could not be found. *Lower panels* depict contour maps of the eigenstates $\psi_{2\text{D}}(R_1, R_2)$ calculated in the 2D single state model and belonging to the progression $(v_{\phi}, 1)_{2\text{D}}$. The layout of all wave functions is the same as in Fig. 5. The 2D states are mixed with states $(v_{\phi} + 4, 0)_{2\text{D}}$; counterparts of those marked $(v_{\phi}, 1)_{2\text{D}}^*$ are shown in Fig. 5.

FIG. 7: *Upper panels*: Frequencies (a) in the major experimental progression, (b) in the progression $(v_\phi, 0, 0)$ in the full calculations, and (c) in the progression $(v_\phi, 0)_{2D}$ in the 2D model. In (b), frequencies are lifted by 50 cm^{-1} ; in (c), the frequency scale is omitted. Arrows emphasize the positions of dips in the progressions. *Lower panels*: Potential of the $3^1A'$ state (d) at $\alpha_{OCO} = 179^\circ$ along the ab initio CI seam and (e) across the Mongolian hat top. Angular coordinate ϕ along the seam in (d) is chosen such that $\phi = 180^\circ$ for $R_1 = R_2 = 2.24 a_0$; the ‘radial’ coordinate in (e) runs along the antisymmetric stretch R_- , and the origin $R_- = 0$ is the point $R_1 = R_2 = 2.5 a_0$. Potential curves are rised through the zero point energies of ‘missing’ coordinates, $\hbar\omega_r/2$ and $\hbar\omega_\phi/2$ in (d) and (e), respectively. Vibrational ladder in the 2D model is indicated in (d) and (e). Energy spacings forming two dips in the progression in panel (c) are highlighted with gray and yellow.

FIG. 8: Shown left of the vertical dashed line are frequencies in the pure progressions of eigenstates Ψ_n in which the $2^1A'$ adiabatic component (purple, blue, and brown lines and symbols) or the $1^1A''$ adiabatic component (red lines and symbols) are most populated. Open black symbols are the two experimental vibrational progressions (triangles and squares), as well as the frequency shift between their band maxima (circles) taken from Table 3 of Ref. 19. Shown right of the vertical dashed line are energy intervals between adjacent diffuse peaks in the experimental spectrum of Ref. 17 (black open circles) and between most intense resonance states (green solid circles). Note that the frequency scale changes in the upper part of the figure.

FIG. 9: $2A'$ adiabatic component of the resonance state with $E_0 = 8.3795 \text{ eV}$ and $\Gamma_0 = 62 \text{ cm}^{-1}$. Shown is one particular contour $|\Psi(R_1, R_2, \alpha_{OCO})|^2 = \text{const.}$, with the same constant in both panels. The contour is viewed along α_{OCO} (left panel) and along the CO bond (right panel). Shading emphasizes the 3D character of the plots. The 2D contour maps of the adiabatic state $2^1A'$ in the (R_1, R_2) plane and in the (α_{OCO}, R_2) plane are sketched in the left and right panels, respectively. Thick black lines trace out the probability density buildup away from the linear FC region.

FIG. 10: $2A'$ adiabatic components of the 3D wave functions of states in the progression $(v_s, 0, 0)$ (upper panels) and $(0, 0, v_a)$ (lower panels). The layout of all wave functions is the same as in the left panel of Fig. 9.

FIG. 11: $2A'$ adiabatic components of the 3D wave functions of states in the progression $(0, v_b, 0)$. In the left lower frame, the ground vibrational state in the carbene-type OCO minimum is shown and labeled $(0, 0, 0)_c$. The layout of all wave functions is the same as in the right panel of Fig. 9.

FIG. 12: Absorption spectrum of the state ${}^1\Sigma_u^-$ and assignments of the three progressions $(v_s, 0, v_a)$ in which the most intense absorption lines are found.

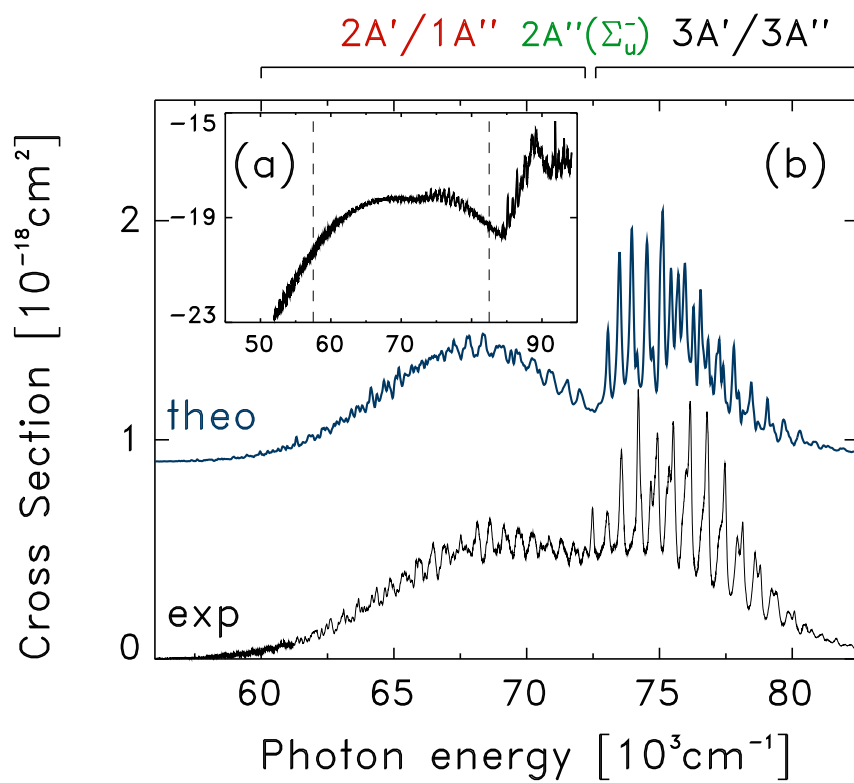


Fig. 1

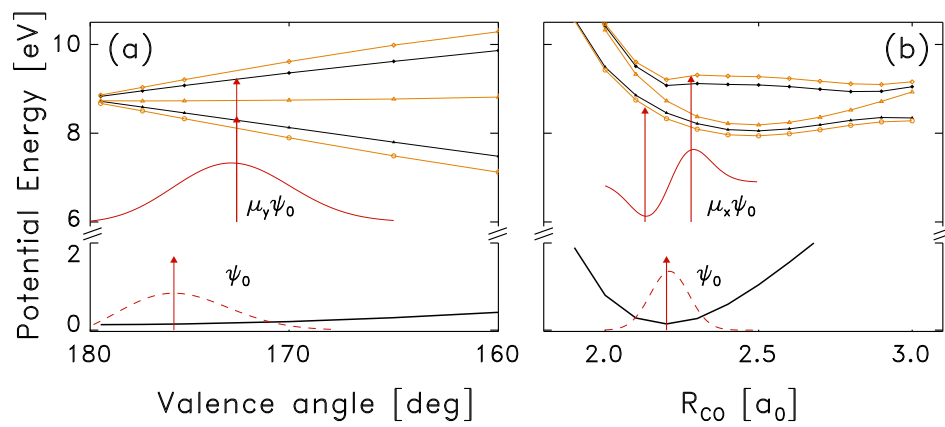


Fig. 2

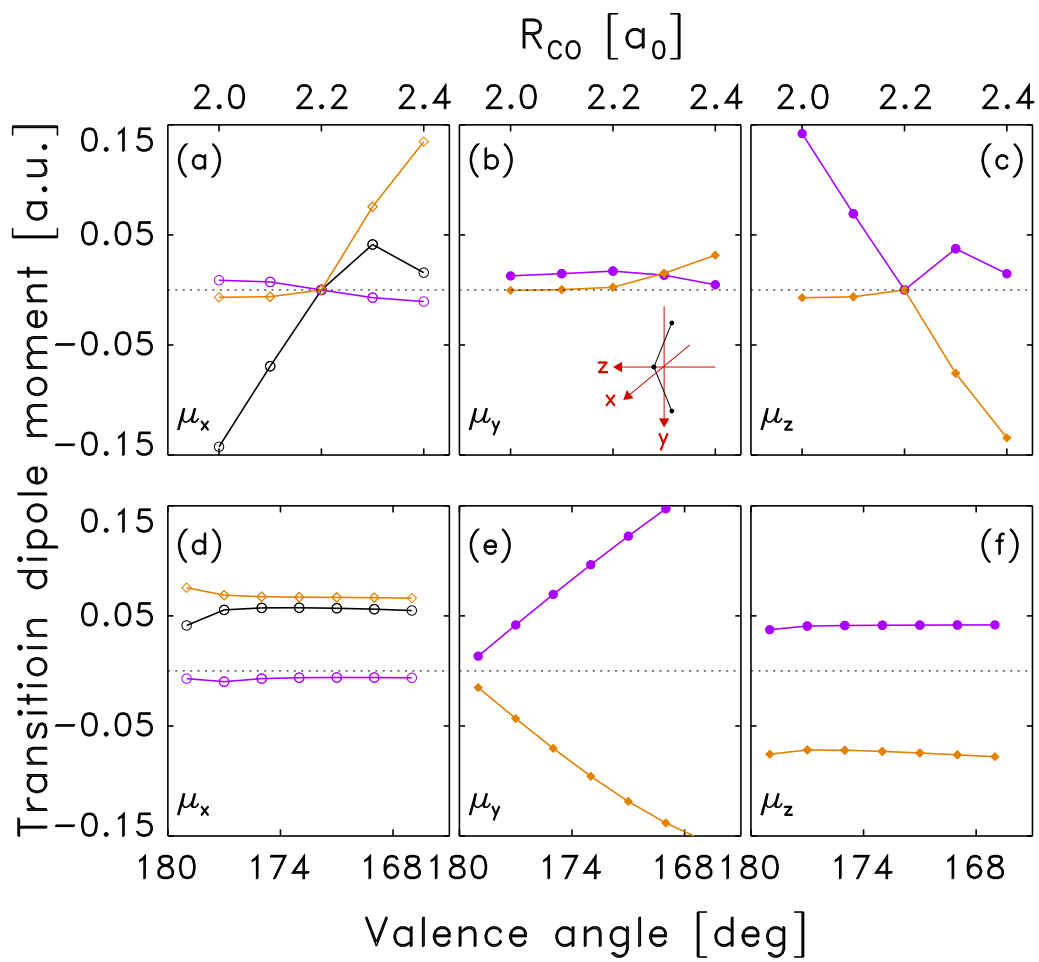


Fig. 3

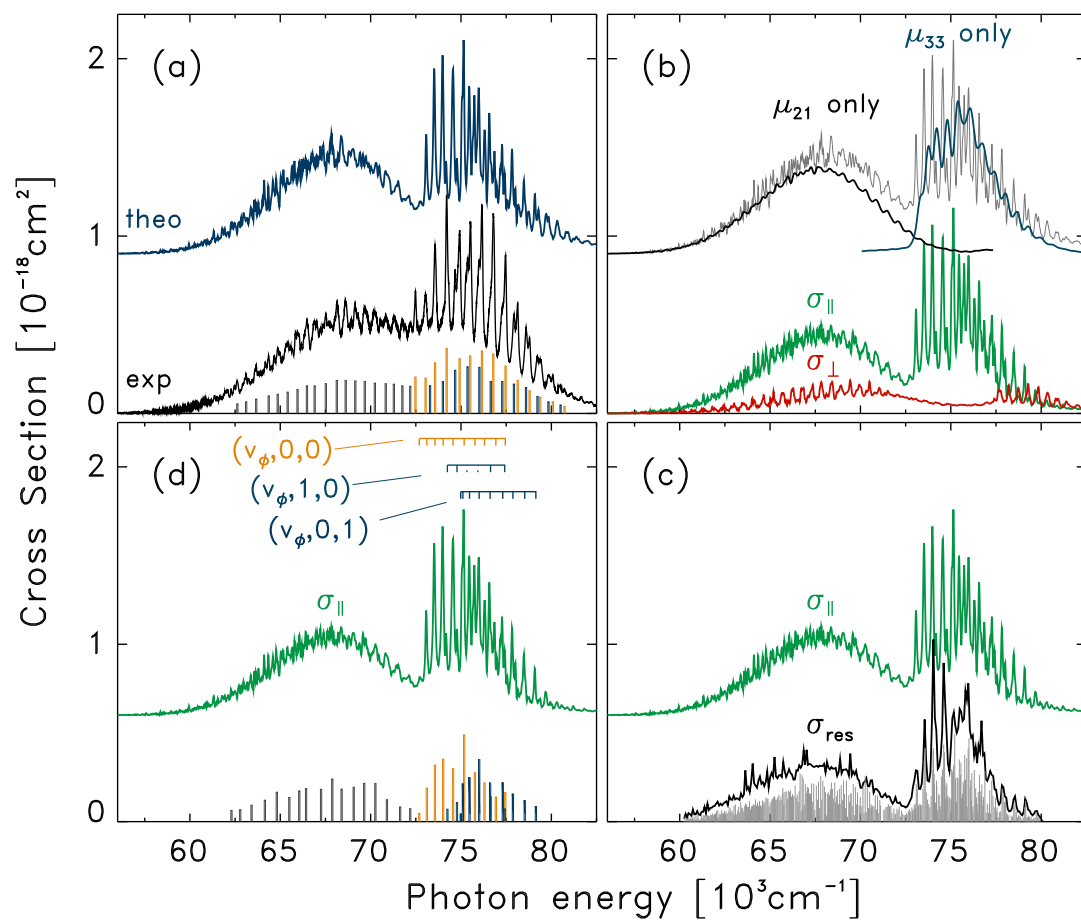


Fig. 4

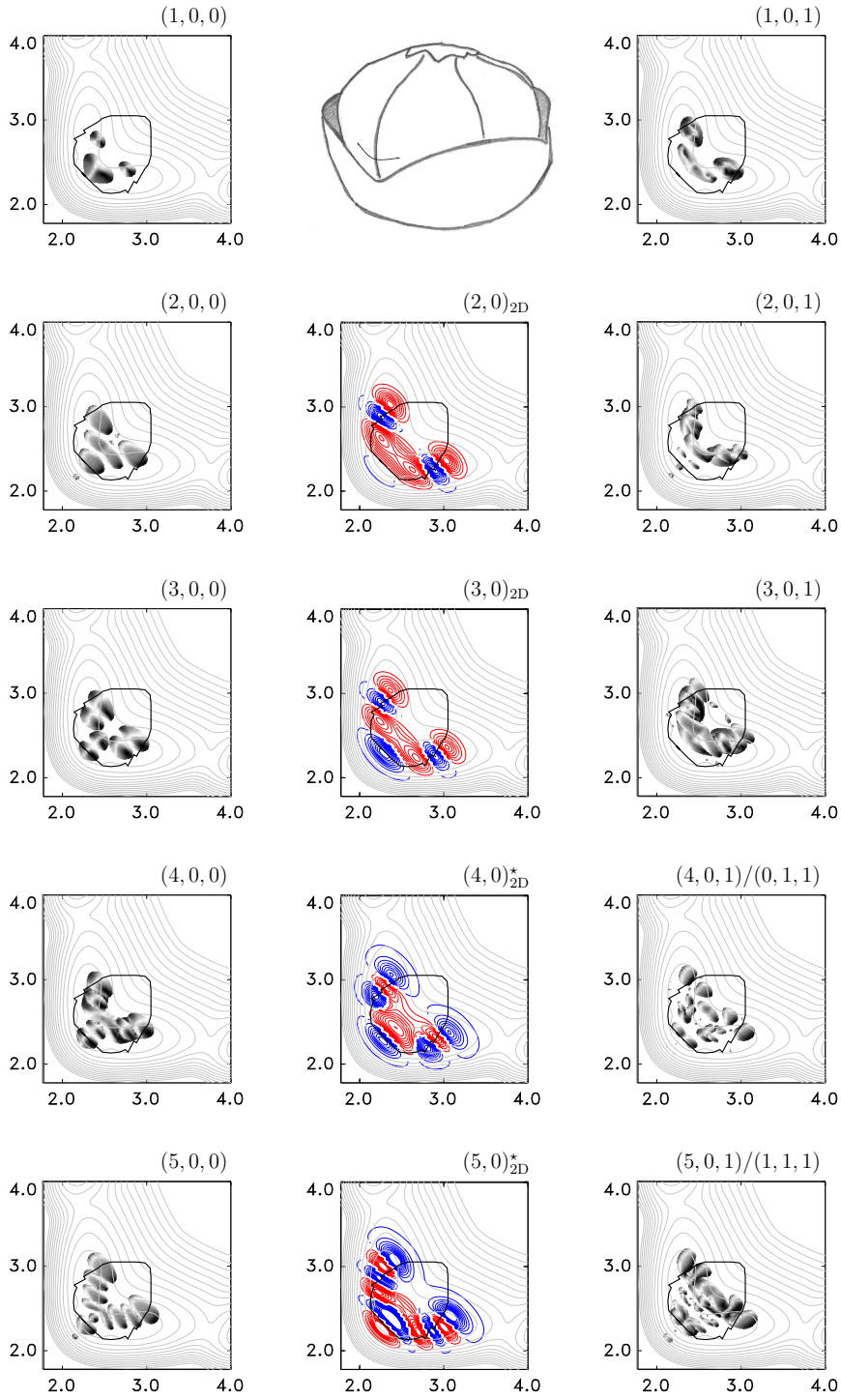


Fig. 5

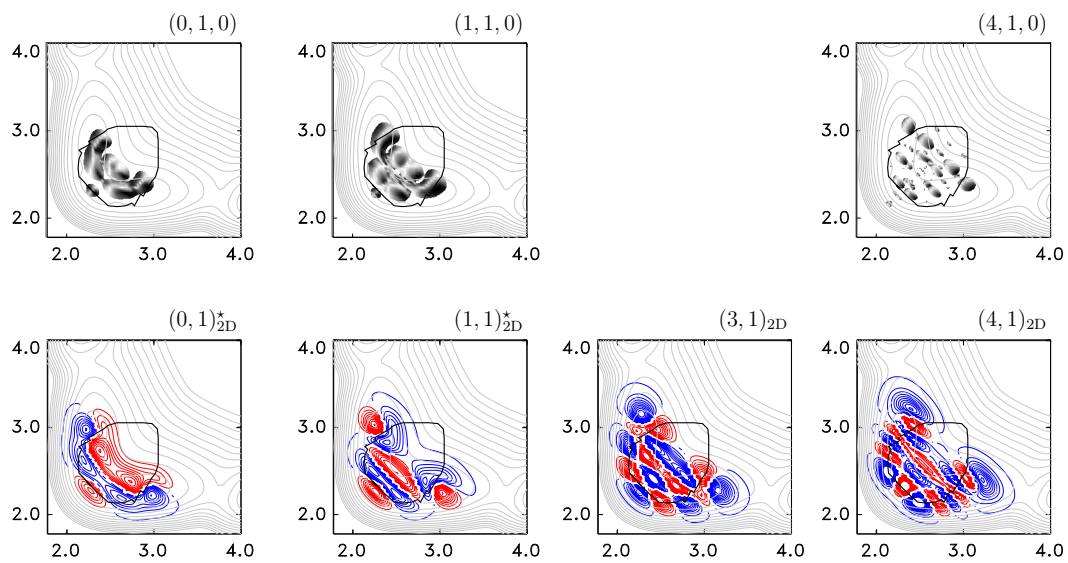


Fig. 6

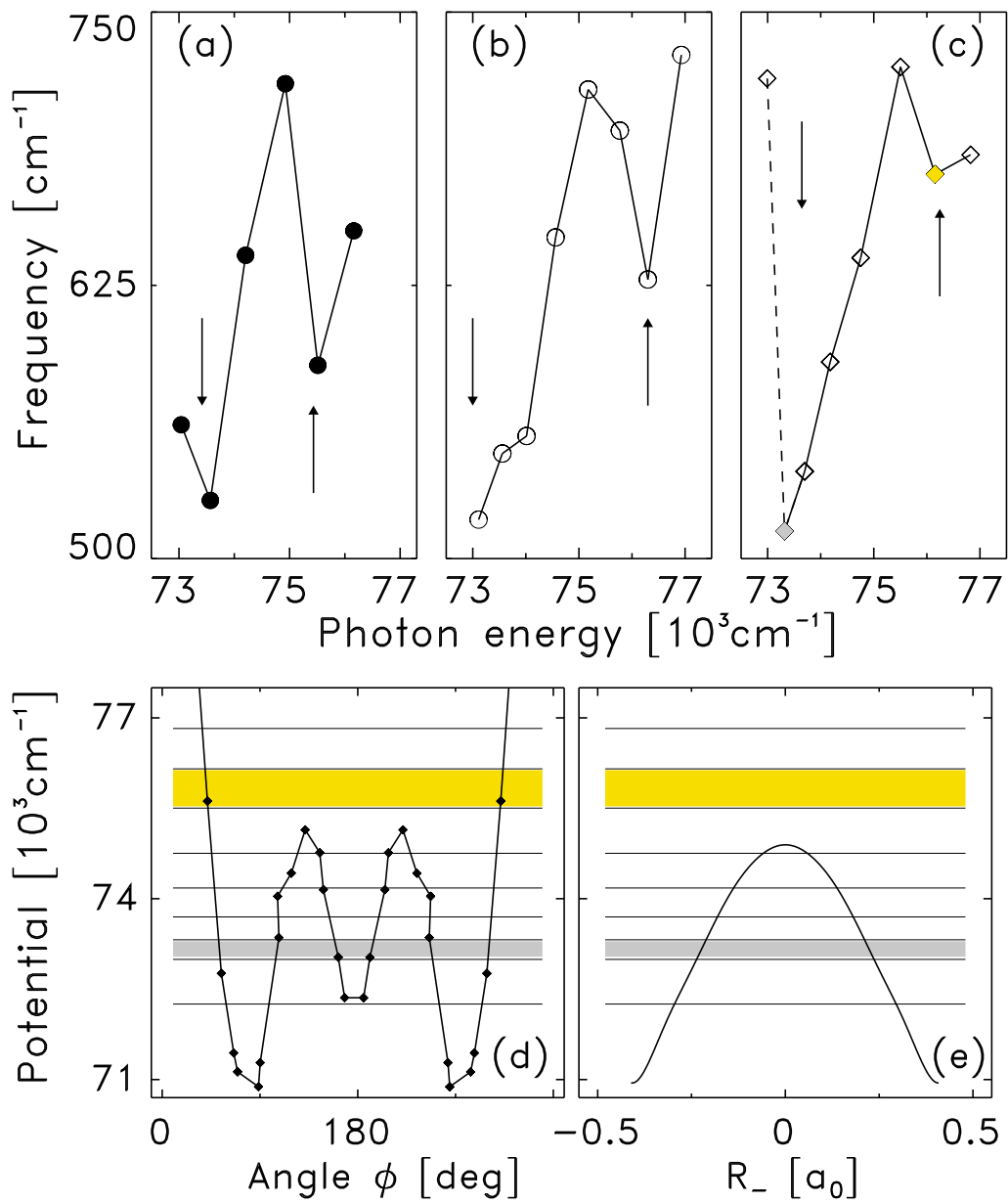


Fig. 7

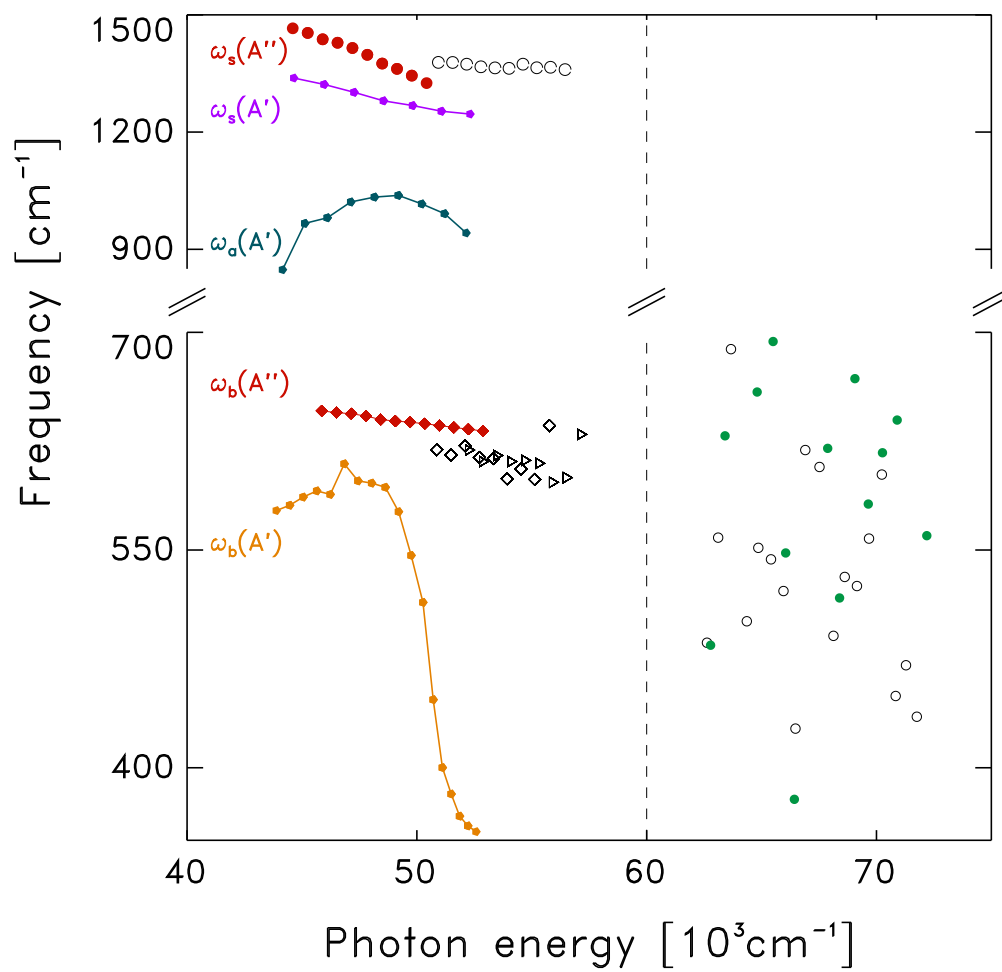


Fig. 8

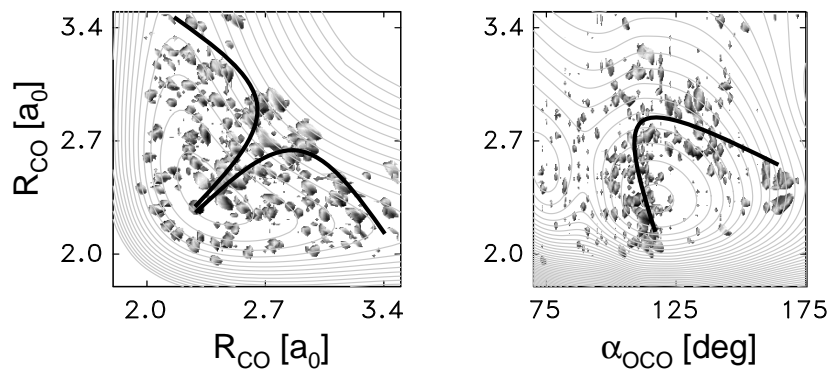


Fig. 9

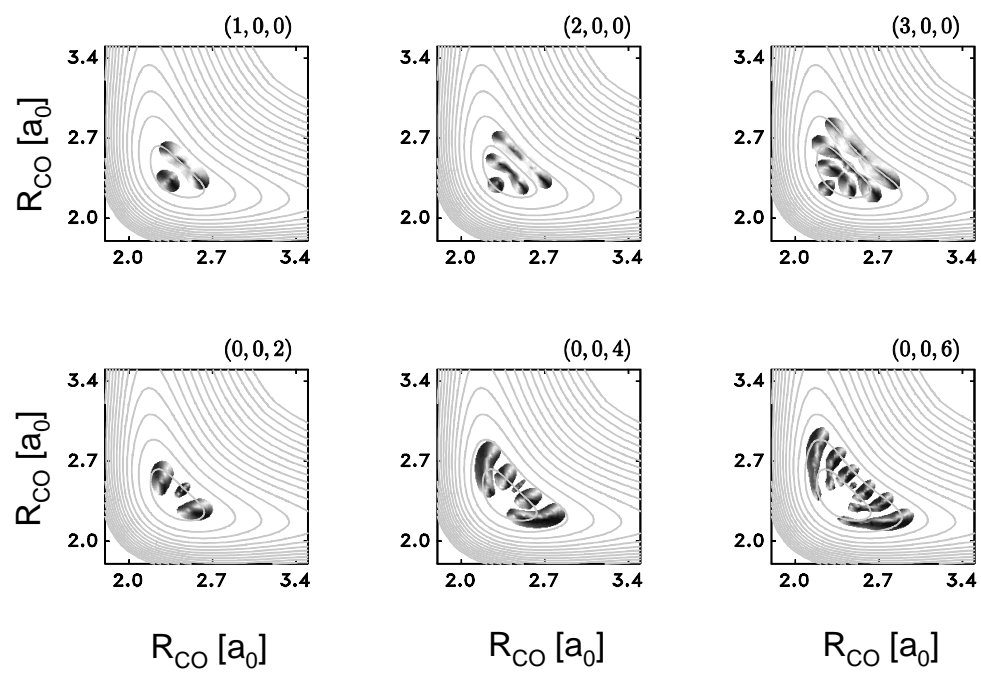


Fig. 10

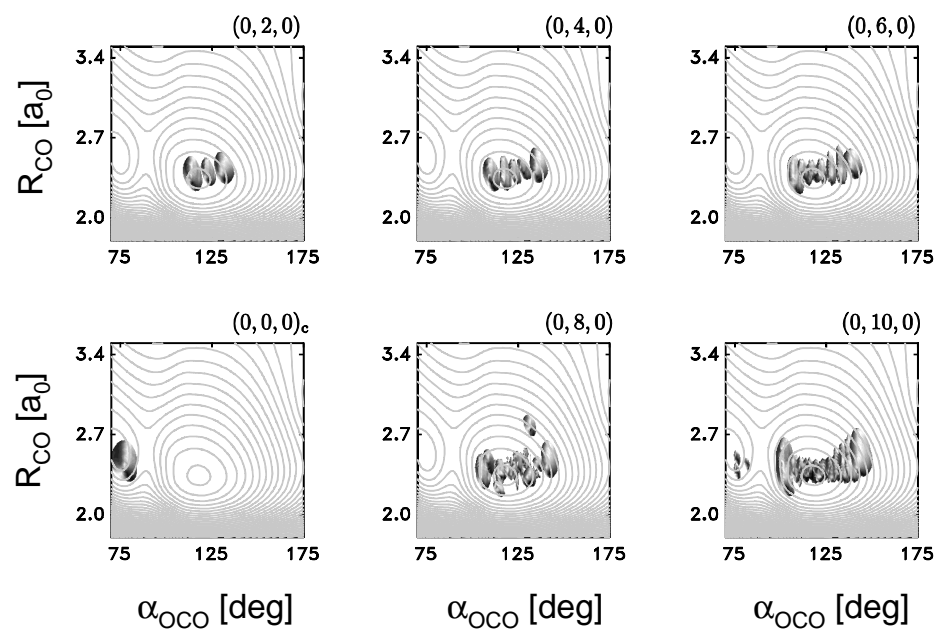


Fig. 11

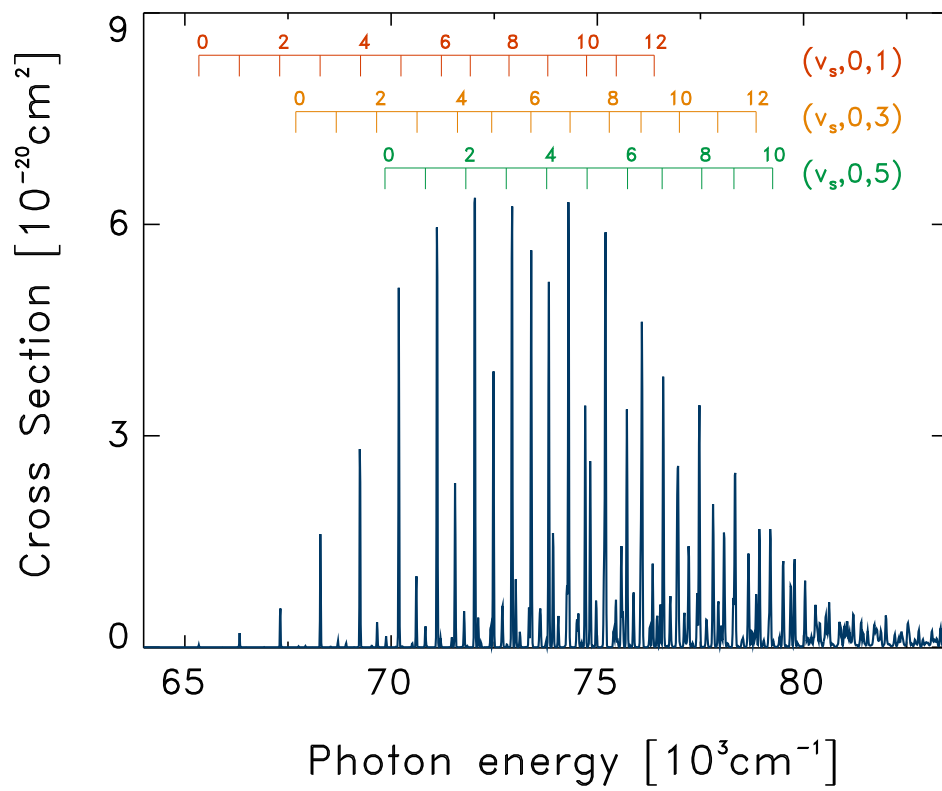


Fig. 12